METHODS TO IMPROVE INDENTATION RESULTS ON SOFT MATERIALS AND ANISOTROPIC BIOLOGICAL TISSUES

BY

JIE WEI

DISSERTATION

Submitted in partial fulfillment of the requirements
for the degree of Doctor of Philosophy in Mechanical Engineering
in the Graduate College of the
University of Illinois at Urbana-Champaign, 2018

Urbana, Illinois

Doctoral Committee:

Professor Amy J. Wagoner Johnson, Chair, Director of Research
Professor Michael Insana
Professor Yuhang Hu
Professor Alison Dunn

ABSTRACT

Mechanical properties of soft biological tissues are key to the functionality of such tissues. Indentation has become a leading technique for characterizing the localized mechanical properties of materials, and it is an increasingly popular technique for studying biological materials. This thesis investigates difficulties and challenges regarding the application of micro-scale indentation.

This study first develops a novel approach, namely the multi-indent approach (MIA), which mitigates the long-standing challenge of surface detection and broadens the use of instrumented indentation for soft materials. The MIA is experimentally validated on isotropic polyacrylamide gel with load-unload cycles in indentation. Furthermore, it is applied to accurate characterization of poroelastic properties and allows for the use of much smaller probes and indentation depths for all measurements.

This study also establishes a corrected method for non-circular contact between a spherical tip and the transversely isotropic material. It develops experimental methods to determine the indentation moduli of a locally transversely isotropic collagenous material as well as the correlation between the aspect ratios (ARs) of contact and correction coefficients for contact areas (RCA).

Lastly, this study designs a method for selecting the spherical tip size for indentation based on the collagen fiber distribution in order to correctly sense the differences of local mechanical properties in heterogeneous tissues caused by the uneven fiber distribution. This thesis introduces methods and results that provide guidance and insight regarding the correct design and analysis of indentation experiments on soft

materials and anisotropic biological tissues.

ACKNOWLEDGEMENTS

Firstly, I would like to express my sincere gratitude to my advisor Prof. Amy Wagoner Johnson for the continuous support of my Ph.D study and related research, for her patience, motivation, and sharing of the knowledge. Her great guidance helped me in all the time of research and writing of this thesis, with her comforting when I was in the plateau of the research, and her cheering when I made accomplishment. Without her great support, this will not be achieved.

Next, I would like to thank the rest of my thesis committee: Prof. Micheal Insana, Prof. Alison Dunn, and Prof. Yuhang Hu, for their insightful comments and encouragement, and also for the question which incented me to widen my research from various perspectives.

Friends and lab mates in UIUC also give me enormous support. My sincere thanks also goes to my fellow lab mates, Laurence Rustom, Zack Bernnet, Ashley Amstrong, and former lab mate Mike Poellman, for the interesting and inspiring discussions, and encouragement we gave to each other. I would also like to acknowledge my friends in UIUC, for all the happy and tough time that we go thru hand in hand.

I would also like to give my thanks to Kathy Smith, who kindly and supportively helped me a lot through the difficulties. My thanks also go to my friend Kate Norcross and her family, Sara Hoag and Lynnette, for being my best friends and sisters. God shed the light into our lives, and bond us together like limbs and legs. Your love makes me stronger and better.

Last, but not the least, I would like to give my special thanks to my family. I remember the happy faces when my parents saw me after 14-hour flight, and the delicious food they made for me when there is still strong jet-lag, I remember my boyfriend Jiabin Zhang, spent whole night comforting me with “take it easy”, and flying to Champaign the next day. Without family, I will never become who I am.

TABLE OF CONTENTS

CHAPTER 1: INTRODUCTION

1.1 MOTIVATION FOR USE OF INDENTATION

Indentation is a common technique to determine the hardness of a material. It monitors the real-time load and indentation depth of a tip with well-defined geometry and employs these data, combined with models, to obtain material properties.[1–4] Indentation measurements can be applicable at the macro-, micro-, or nano-scale depending on the forces and displacements in use.

Indentation at the macro-scale hardness of materials is a quick and simple method to obtain mechanical property data for the bulk material from a small sample. It is also widely used for quality control of surface treatment processes. However, when concerned with coatings and important surface properties for friction and wear processes, for instance, the macro-indentation depth is too large in relation to the surface-scale features, so a smaller-scale indentation is needed.[4–7]

Micro-indentation tests the indentation hardness of a material by forcing an indenter, such as a Vickers or Knoop indenter, into the surface of the material under 0.1N to 10N load.[3,8–10] On the micro-scale, the indentation marks are so small that they must be measured with a microscope. Micro-indentation is capable of measuring the hardness of different micro-constituents within a structure, and the microscopic hardness of the material can be converted to the microscopic tensile strength or other hardness on macro-scales (e.g. Rockwell). Many metals and alloys have been studied with micro-indentation,[11,12] and it has also been applied to hard biological tissues, such as bone.[13–16]

Indentation is additionally used to investigate the indentation modulus of soft materials. Macro-indentation on soft materials has been studied with soft polyacrylamide gels[7,17–19] and

biological tissues.[6,17,20,21] Micro-indentation is especially useful for differentiating properties over small regions, e.g. an area of several micrometers, through the use of probe sizes that range from 10μm to 1mm as well as high force and displacement resolution (less than 1nN, 1nm).[22,23] Thus, indentation has been increasingly recognized as an efficient approach to understanding the biological process of diseased or damaged tissues.[5,10,24] Few studies have used micro-indentation to study soft tissues whose moduli are less than 1MPa.[10,18,25,26] For example, Yao et al. have characterized the shear modulus and poroelastic properties of the human cervix,[27] Slaboch et al. typified rat thrombus relaxation behavior with indentation,[28] Chhetri et al. have studied elastic properties of vocal folds,[29] and Gupta et al. have defined porcine cartilage time-independent properties.[30]

1.1.1 Indentation devices

Indentation tests have commonly used two major types of indentation systems: instrumented indentation and cantilever-based indentation, which includes atomic force microscopy (AFM). Figure 1A[24,31–33] depicts a schematic of the former, while Figure 1B[20,34,35] illustrates the latter.

Cantilever-based indentation uses optical interferometry to measure the deflection at the end of a cantilever beam that has a tip installed, and it calculates the load according to the calibrated stiffness of the cantilever.[20,34,35] The research presented in Chapter 5 utilized a commercial cantilever-based indenter with a 9-μm indenter tip that was made by Piuma Inc., Netherlands.

Instrumented indentation is also known as depth-sensing indentation. It enables the measurement of the displacement of a probe along with the load during contact with the material surface. The elastic modulus of the probe is usually much larger than that of the sample.[24,31–33]

Typically, instrumented indentation is capable of measuring displacement of a couple of microns or tens of microns. The TI-950 Hysitron Tribo-indenter is a commonly employed instrumental indentation device that was used in one of the experimental approaches in Chapters 3 and 5.

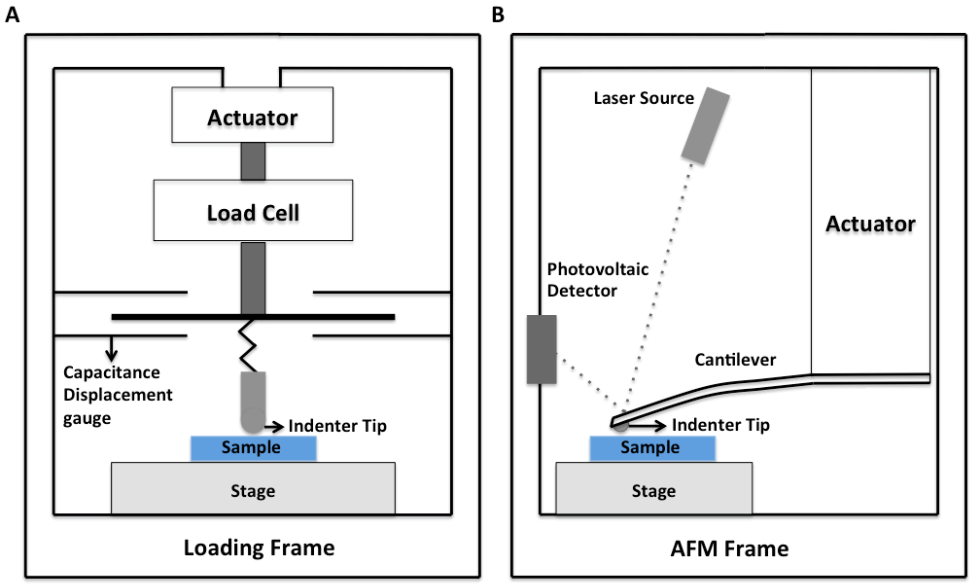

Figure 1 (A) Schematic of the working principal of a typical instrumented indenter; the load and displacement sensors are placed in alignment with the direction of indentation (B) Schematic of the working principal of a typical cantilever-based indenter; displacement is controlled at the actuator side, which is the tip-less end of the cantilever

1.2 CHALLENGES IN INDENTATION OF SOFT MATERIALS

1.2.1 Challenge in surface detection

Detecting the sample surface is arguably one of the most crucial challenges in determining accurate material properties with currently available commercialized indenters. For soft materials, the preload must be sufficiently large to register contact with the material surface. With too small of a preload, the tip-fluid interaction can trigger false engagement, or false engagement can be triggered before full contact is made. With such large preloads, the indentation test typically starts from a deformed surface, i.e. with the probe at some initial preload-induced indentation depth that is below the undeformed surface. This is especially

relevant for systems with a small retraction distance of approximately 150 nm. This initial indentation depth can be on the order of microns. There is currently no non-destructive method to determine the initial depth, and the result is an overestimation of properties such as Young's modulus and shear modulus.

Previous studies have suggested tracking the surface deformation with florescent particles as a means to resolve the surface detection problem.[36] This method requires specialized equipment, and not all materials can be prepared with fluorescent beads on the surface. Li et al. and Bhushan et al. have proposed surface detection by monitoring the change in stiffness through cyclic loading; however, the theory was developed for rigid plastic materials.[37] This approach is not applicable to viscoelastic and viscoelastic-plastic materials because it does not account for time-dependent behavior. Ebenstein et al. have examined surface detection through dynamic testing. High-frequency dynamic testing can result in sample heating, which in turn can cause softening or even melting.[38] Other studies have not addressed the surface detection problem at all. Chapter 3 further discusses the technical challenge of surface detection in indentation.

1.2.2 Challenge in estimating the contact area on transversely isotropic collagenous tissue

Transversely isotropic materials have material properties in the second and third principal directions that are the same.[39–41] A low degree of anisotropy entails that the material properties, such as elastic modulus, shear modulus, and Poisson's ratio, have nearly the same values in each principal direction. A high degree of anisotropy in transversely isotropic materials conveys that the elastic modulus, shear modulus, and Poisson's ratio in the two principal directions can be drastically different.[39,40,42]

The estimation of contact area is a key step in obtaining an accurate indentation

modulus.[17,43] Determining the contact between a rigid spherical indenter and a transversely isotropic heterogeneous collagenous tissue requires a method of determining the contact at the local region of the material. For transversely isotropic materials, two types of contact models to describe anisotropic material behavior have usually been used: the circular contact approximation and the elliptical contact model.[44–46] The circular approximation is easy in calculation[44,47] but is only suitable for fiber reinforced materials with low degree of anisotropy.[44,47] The elliptical contact model is more accurate for determining contact area and is usually numerically solved.[44,47] Both models require the knowledge of material properties in three principal directions of the material. In order to apply the elliptical theory, the tensile modulus along and perpendicular to the material symmetry axis needs to be evaluated through uniaxial tensile tests.[40–42] However, many collagenous tissues are both heterogeneous and anisotropic.[48,49] Measuring the local tensile modulus in these cases is highly difficult, if not impossible. Therefore, locally estimating the contact area for such complex tissues is challenging. Chapter 4 elaborates on the issue of estimating the non-circular contact.

1.2.3 Challenge in determining the tip size for indentation

Biological tissues, including those of the cervix and tendons, are fiber-reinforced soft tissues. They can be described as a composite of a homogeneous isotropic solid matrix with collagen fibers distributed in it. Natural tissues are hierarchically structured materials that exhibit a variety of structural and mechanical characteristics in fibers over a range of length scales.[6,18,50] As a consequence of their varied structure, these tissues exhibit different mechanical properties at different length scales.

The indentation modulus on the same tissue is reported in a wide range, and a variety of tip sizes have been used.[8,14,51] Since the size of the tip may lead to disparate results of the

indentation modulus, the selection of the tip size is critical in terms of its association to the underlying fiber distribution structures. Chapter 5 addresses tip size effects based on fiber dimension and structure analyses.

1.3 THESIS ORGANIZATION

1.3.1 Thesis motivation

The present work aims to characterize soft materials and biological tissues by means of indentation. For this purpose, theoretical and technological limitations that relate to the indentation of soft isotropic materials were investigated with a commercial nanoindenter (Hysitron TriboIndenter) that is frequently employed for the indentation of hard materials. In addition to difficulties concerning the experimental procedure, the analysis of experimental data for anisotropic material by reliable models is critical to accurately characterize the mechanical response of the material under indentation tests. The following chapters investigate these yet-unresolved difficulties and limitations.

1.3.2 Thesis Outline

Chapter 2, "Theories," identifies the theories that have informed this thesis and its analysis.

Chapter 3, "Multi-indent approach to detect the surface of soft materials during indentation," addresses the challenges of surface detection that were noted in Section 1.2.1. It specifically develops a novel method to estimate the true indentation depth and indentation modulus.

Chapter 4, "Method to determine non-circular contact and elastic moduli of transversely isotropic collagenous tissue using indentation," contends with the challenges in estimating the contact for anisotropic materials as described in Section 1.2.2. To this end, it develops a method

to acquire images of non-circular contact for transversely isotropic collagenous tissue. These images are used to determine the AR of the non-circular contact and then to obtain a better measure of the local indentation modulus.

Chapter 5, "Method to choose correct tip size based on the fiber dimension and structure," approaches the challenge of choosing a tip size in relation to the fiber distribution characteristics that was explained in Section 1.2.3. This chapter also exemplifies how the methods that Chapters 3 and 4 develop can be applied to an anisotropic biological tissue.

Chapter 6 concludes the work and specifies the contributions of this thesis.

1.4 REFERENCES

1. Oyen, M. L. Analytical techniques for indentation of viscoelastic materials. Philosophical Magazine **86,** 5625–5641 (2006).
2. Oliver, W. C. & Pharr, G. M. Measurement of hardness and elastic modulus by instrumented indentation: Advances in understanding and refinements to methodology. Journal of Materials Research **19,** 3–20 (2004).
3. Vlassak, J. J. & Nix, W. D. Indentation modulus of elastically anisotropic half spaces. Philosophical Magazine A **67,** 1045–1056 (1993).
4. Kalcioglu, Z. I., Mahmoodian, R., Hu, Y., Suo, Z. & Van Vliet, K. J. From macro- to microscale poroelastic characterization of polymeric hydrogels via indentation. Soft Matter **8,** 3393 (2012).
5. McKee, C. T., Last, J. a, Russell, P. & Murphy, C. J. Indentation versus tensile measurements of Young's modulus for soft biological tissues. Tissue engineering. Part B, Reviews **17,** 155–164 (2011).

6. Iivarinen, J. T., Korhonen, R. K. & Jurvelin, J. S. Experimental and numerical analysis of soft tissue stiffness measurement using manual indentation device - significance of indentation geometry and soft tissue thickness. Skin Research and Technology **20,** 347–354 (2014).

7. Hu, Y., Chan, E. P., Vlassak, J. J. & Suo, Z. Poroelastic relaxation indentation of thin layers of gels. Journal of Applied Physics **110,** 13–16 (2011).

8. Chardon, M. K., Rymer, W. Z. & Suresh, N. L. Quantifying the deep tendon reflex using varying tendon indentation depths: Applications to spasticity. IEEE Transactions on Neural Systems and Rehabilitation Engineering **22,** 280–289 (2014).

9. Clayton, J. D. Spherical Indentation in Elastoplastic Materials : Modeling and Simulation. (2005).

10. Genovese, K., Montes, A., Martínez, A. & Evans, S. L. Full-surface deformation measurement of anisotropic tissues under indentation. Medical Engineering and Physics **37,** 484–493 (2015).

11. Kramer, D. E., Volinsky, A. A., Moody, N. R. & Gerberich, W. W. Substrate effects on indentation plastic zone development in thin soft films. Journal of Materials Research **16,** 3150–3157 (2001).

12. Ebenstein, D. M. & Wahl, K. J. A comparison of JKR-based methods to analyze quasi-static and dynamic indentation force curves. Journal of colloid and interface science **298,** 652–62 (2006).

13. Paietta, R. C., Campbell, S. E. & Ferguson, V. L. Influences of spherical tip radius, contact depth, and contact area on nanoindentation properties of bone. Journal of Biomechanics **44,** 285–290 (2011).

14. Spiesz, E. M., Roschger, P. & Zysset, P. K. Elastic anisotropy of uniaxial mineralized collagen fibers measured using two-directional indentation. Effects of hydration state and indentation depth. Journal of the mechanical behavior of biomedical materials **12,** 20–8 (2012).

15. Galli, M. & Oyen, M. L. Fast identification of poroelastic parameters from indentation tests. CMES - Computer Modeling in Engineering and Sciences **48,** 241–269 (2009).

16. Hauch, K. N., Oyen, M. L., Odegard, G. M. & Haut Donahue, T. L. Nanoindentation of the insertional zones of human meniscal attachments into underlying bone. Journal of the mechanical behavior of biomedical materials **2,** 339–47 (2009).

17. Lin, D. C., Shreiber, D. I., Dimitriadis, E. K. & Horkay, F. Spherical indentation of soft matter beyond the Hertzian regime: Numerical and experimental validation of hyperelastic models. Biomechanics and Modeling in Mechanobiology **8,** 345–358 (2009).

18. Wang, Q. M., Mohan, A. C., Oyen, M. L. & Zhao, X. H. Separating viscoelasticity and poroelasticity of gels with different length and time scales. Acta Mechanica Sinica/Lixue Xuebao **30,** 20–27 (2014).

19. Cai, S., Hu, Y., Zhao, X. & Suo, Z. Poroelasticity of a covalently crosslinked alginate hydrogel under compression. Journal of Applied Physics **108,** 1–8 (2010).

20. Heris, H. K., Miri, A. K., Tripathy, U., Barthelat, F. & Mongeau, L. Indentation of poroviscoelastic vocal fold tissue using an atomic force microscope. Journal of the mechanical behavior of biomedical materials **28,** 383–92 (2013).

21. Lake, S. P. & Barocas, V. H. Mechanics and kinematics of soft tissue under indentation are determined by the degree of initial collagen fiber alignment. Journal of the Mechanical Behavior of Biomedical Materials **13,** 25–35 (2012).

22. Bhattacharya, a. K. & Nix, W. D. Finite element simulation of indentation experiments. International Journal of Solids and Structures **24,** 881–891 (1988).

23. Karimzadeh, a., Ayatollahi, M. R. & Alizadeh, M. Finite element simulation of nano-indentation experiment on aluminum 1100. Computational Materials Science **81,** 595–600 (2014).

24. Farine, M. Instrumented Indentation of Soft Materials and Biological Tissues. (2013).

25. Yao, W. et al. Measuring the compressive viscoelastic mechanical properties of human cervical tissue using indentation. Journal of the Mechanical Behavior of Biomedical Materials **34,** 18–26 (2014).

26. Nayar, V. T., Weiland, J. D., Nelson, C. S. & Hodge, A. M. Elastic and viscoelastic characterization of agar. Journal of the mechanical behavior of biomedical materials **7,** 60–8 (2012).

27. Yao, W. et al. Collagen fiber orientation and dispersion in the upper cervix of non-pregnant and pregnant women. PLoS ONE **11,** 1–20 (2016).

28. Slaboch, C. L., Alber, M. S., Rosen, E. D. & Ovaert, T. C. Mechano-rheological properties of the murine thrombus determined via nanoindentation and finite element modeling. Journal of the mechanical behavior of biomedical materials **10,** 75–86 (2012).

29. Chhetri, D. K., Zhang, Z. & Neubauer, J. Measurement of Young's modulus of vocal folds by indentation. Journal of Voice **25,** 1–7 (2011).

30. Gupta, S., Lin, J., Ashby, P. & Pruitt, L. A fiber reinforced poroelastic model of nanoindentation of porcine costal cartilage: a combined experimental and finite element approach. Journal of the mechanical behavior of biomedical materials **2,** 326-37–8 (2009).

31. Bhat, T. S. & Venkatesh, T. A. 3-D Finite Element Analysis of Instrumented Indentation

of Transversely Isotropic Materials. Simulia Customer Conference 3–7 (2010).

32. Vanlandingham, M. R. Review of Instrumented Indentation. Journal Of Research Of The National Institute Of Standards And Technology **108,** 249–265 (2003).

33. Lan, H. & Venkatesh, T. a. Determination of the elastic and plastic properties of materials through instrumented indentation with reduced sensitivity. Acta Materialia **55,** 2025–2041 (2007).

34. Calabri, L., Pugno, N., Menozzi, C. & Valeri, S. AFM nanoindentation: tip shape and tip radius of curvature effect on the hardness measurement. Journal of Physics: Condensed Matter **20,** 474208 (2008).

35. Crick, S. L. & Yin, F. C.-P. P. Assessing micromechanical properties of cells with atomic force microscopy: importance of the contact point. Biomechanics and modeling in mechanobiology **6,** 199–210 (2007).

36. Chippada, U., Yurke, B. & Langrana, N. a. Simultaneous determination of Young's modulus, shear modulus, and Poisson's ratio of soft hydrogels. Journal of Materials Research **25,** 545–555 (2010).

37. Li, X. & Bhushan, B. A review of nanoindentation continuous stiffness measurement technique and its applications. Science **48,** 11–36 (2002).

38. Kohn, J. C. & Ebenstein, D. M. Eliminating adhesion errors in nanoindentation of compliant polymers and hydrogels. Journal of the mechanical behavior of biomedical materials **20,** 316–26 (2013).

39. Morrow, D. A., Haut Donahue, T. L., Odegard, G. M. & Kaufman, K. R. Transversely isotropic tensile material properties of skeletal muscle tissue. Journal of the mechanical behavior of biomedical materials **3,** 124–9 (2010).

40. Yin, L. & Elliott, D. M. A biphasic and transversely isotropic mechanical model for tendon: Application to mouse tail fascicles in uniaxial tension. Journal of Biomechanics **37,** 907–916 (2004).

41. Dahan, M. & Zarka, J. Elastic contact between a sphere and a semi infinite transversely isotropic body. International Journal of Solids and Structures **13,** 229–238 (1977).

42. Willis, J. R. HERTZIAN CONTACT OF ANISOTROYIC BODIES. J. Mech. Phys. Solids **14,** 163–176 (1966).

43. Noël, C. F. O., Charles, I. & Cnrs, S. Extension of the Hertz model for accounting to surface tension in nano- indentation tests of soft materials. Assessment 13–17 (2007).

44. Swanson, S. R. Hertzian contact of orthotropic materials. International Journal of Solids and Structures **41,** 1945–1959 (2004).

45. Pareja, N. V. R. Contact and Friction in Systems with Fibre Reinforced Elastomers. Tribology and Surface Technology **PhD,** (2011).

46. Tan, T. M. & Sun, C. T. Use of Statical Indentation Laws in the Impact Analysis of Laminated Composite Plates. ASME **52,** (1985).

47. Wald, M. J., Considine, J. M. & Turner, K. T. Indentation measurements on soft materials using optical surface deformation measurements. Mechanics of Biological Systems **4,** 41–51 (2014).

48. Flynn, C. A model for the anisotropic response of fibrous soft tissues using six discrete fibre bundles Short.

49. Gan, Y. et al. Analyzing three-dimensional ultrastructure of human cervical tissue using optical coherence tomography. Biomedical Optics Express **6,** 1090 (2015).

50. Ebenstein, D. M. & Pruitt, L. a. Nanoindentation of biological materials. Nano Today **1,**

26–33 (2006).

51. Chardon, M. K., Dhaher, Y. Y., Suresh, N. I., Jaramillo, G. & Zev Rymer, W. Estimation of musculotendon kinematics under controlled tendon indentation. Journal of Biomechanics **48,** 3577–3585 (2015).

CHAPTER 2: CONTACT THEORIES

A key influential factor in the indentation process is the interaction of the indenter tip with the test material. In this regard, previous research has extensively documented contact theories. This section provides an introduction to such theories.

2.1 ISOTROPIC CONTACT THEORIES

2.1.1 Hertzian contact between sphere and a half-plane

The contact solution for two deformable and frictionless homogeneous elastic bodies is well developed.[1–3] When an elastic sphere of radius R, here a spherical indenter, indents on elastic half-space with a contact area of radius a, the contact radius relates to the R and the indentation depth d (Equation 1).[1,4]

$$a = \sqrt{Rd} \quad (1)$$

The force that is applied to the sample follows Equation 2, where k is a coefficient relating to R and the indentation modulus E*. Equation 3 and Equation 4 express this modulus, which relates to the indenter properties E_i and v_i as well as to the sample properties E_s and v_s. If the indenter is much stiffer than the sample, then E* can be expressed as Eqn5. The shape of the two contact entities determines the exponent q, which is a shape factor. For the elastic contact between a sphere and a half-plane, q = 1.5. Equation 6 illustrates the expression of total contact force.[5] This study uses this form.[2,6]

$$F = kd^q \quad (2)$$

$$k = \frac{4}{3} E^* R^{1/2} \quad (3)$$

$$\frac{1}{E^*} = \frac{1 - v_s^2}{E_s} + \frac{1 - v_i^2}{E_i} \quad (4)$$

$$\frac{1}{E^*} = \frac{1 - v_s^2}{E_s} (5)$$

$$F = \frac{4}{3} E^* R^{1/2} d^{3/2} (6)$$

Equations 1 through 4 yield an expression for the contact radius as a function of the total force, indenter radius, and the indentation modulus. Equation 7 presents the final expression for the contact radius.

$$a = \sqrt[3]{\frac{3FR}{4E^*}} (7)$$

2.1.2 Oliver-Pharr model

The method that this study introduces, namely the multi-indent approach (MIA), derives from the popular Oliver-Pharr model.[7] The Oliver-Pharr model has been most widely applied to elastic materials with a Young's modulus greater than 1MPa. It has been less commonly used for materials with a modulus between 50kPa and 1MPa, and even more rarely for softer materials.[4] In order to introduce specific concepts and notation that relate to the MIA, Figure 2 and Equations 1 through 7 provide an overview of the Oliver-Pharr model.

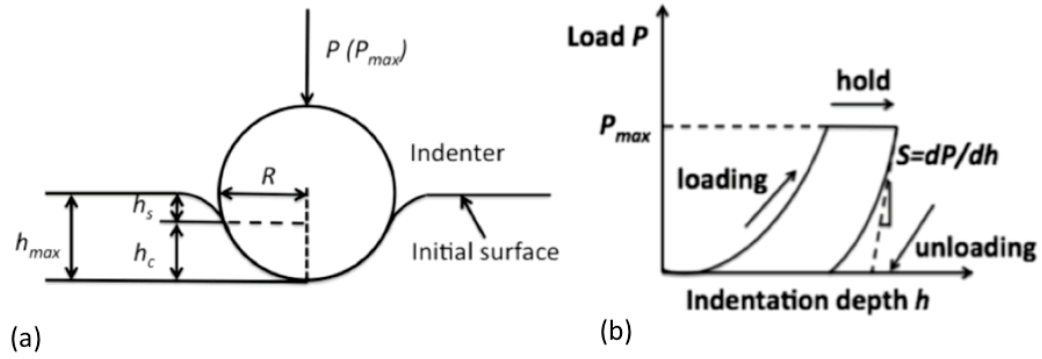

Figure 2. Schematics depicting (a) the geometry of the indentation and (b) the corresponding load-displacement curve during loading and unloading; adapted from Oliver-Pharr[7]

Figures 2A and 2B are schematics of the geometry of indentation and the resultant load-displacement curve during loading and unloading, respectively. During the indentation experiment, the probe continuously indents the material to the maximum load, P_{max}, and maximum indentation depth, h_{max} (Figure 2). The depth over which the indenter is in contact with the material is the contact depth, h_c (Figure 2A). The distance from the contact separation point to the non-deformed surface of the sample is the "sink-in" depth, which is denoted as h_s (Figure 2). It is expressed in Equation 8,[7] where ε is a constant that depends on the geometry of the indenter and is equal to 0.75 for a spherical probe.[7,4] The sum of the sink-in depth and the contact depth is the maximum depth of the indenter, and Equation 9 defines their relationship.

The projected or contact area A of the spherical indenter, which is in contact with the material, depends on the contact depth according to Equation 10, where R is the radius of the spherical indenter tip.[7] The contact area is involved in the calculation of the Young's modulus of the sample, E_s, in Equations 11 through 13.

$$h_s = \varepsilon \frac{P_{max}}{S} \quad (8)$$

$$h_c = h_{max} - \varepsilon \frac{P_{max}}{S} \quad (9)$$

$$A = \pi\left(2Rh_c - {h_c}^2\right) \quad (10)$$

The slope of the unloading curve evaluated at P_{max} is the contact stiffness S, which is illustrated in Figure 1B and expressed by Equation 11. It is a function of the indentation modulus E* the contact area A and a geometric constant β, which has an approximate value of one for the spherical indenter.[7] The modulus of the sample and that of the indenter are contained within Equation 12 for the effective modulus, where the subscript s refers to the properties of the sample, and i represents those of the indenter. Thus, E_s and E_i are the modulus of the sample and

indenter, respectively. Likewise, v_s and v_i are the Poisson's ratio of the sample and the indenter, respectively.

$$S = \beta \frac{2}{\sqrt{\pi}} \sqrt{A}\, E^* \quad (11)$$

$$\frac{1}{E_{eff}} = \frac{1-{v_s}^2}{E_s} + \frac{1-{v_i}^2}{E_i} \quad (12)$$

$$E_{eff} = \frac{E_s}{(1-{v_s}^2)} \quad (13)$$

The indenter that was used for this research was sapphire and had a Young's modulus of 345GPa, while the materials of interest all had a modulus far below 100kPa. Therefore, the second term of Equation 12 is small and negligible, which leaves E_{eff} in the form of Equation 13. Substituting h_c, A, and E_{eff} from Equations 9, 10, and 13, respectively, into Equation 11 yields Equation 14:

$$S = \beta \frac{2}{\sqrt{\pi}} \frac{E_s}{(1-{v_s}^2)} \sqrt{\pi \left(2R\left(h_{max} - \varepsilon \frac{P_{max}}{S}\right) - (h_{max} - \varepsilon \frac{P_{max}}{S})^2\right)} \quad (14)$$

2.2 TRANSVERSELY ISOTROPIC CONTACT THEORIES

2.2.1 Circular contact approximation

Turner has presented a general and convenient solution to determine the contact radius for transversely isotropic contact problems. The approach uses formulae that are similar to those that are utilized for isotropic contact problems.[1,8] Equation 15 gives the modulus in Turner's solution, which is the equivalent transversely isotropic modulus E_{equ} instead of the isotropic indentation modulus E^* from Equation 14.

$$a = \sqrt[3]{\frac{3FR}{4E_{equ}}} \quad (15)$$

E_{equ} relates to the five material parameters that characterize a transversely isotropic material. E_1 and v_1 are the elastic modulus and Poisson's ratio in the first principal direction x in the contact plane, and E_2, v_2 are the elastic modulus and Poisson's ratio in the second principal direction y. In this study, $v_1 = v_2 = v$, while G is the shear modulus of the material. Equations 16 and 17 provide E_{equ}.[1,9]

$$E_{equ} = \frac{2}{\alpha\beta} \qquad (16)$$

$$\alpha = \left(\frac{E_2/E_1 - v^2}{1 - v^2}\right)^{1/2} \quad \text{and} \quad \beta = \frac{1 + \left(\frac{E_1}{2G} - 1\right) - v(1+v)}{1 - v^2} \qquad (17)$$

2.2.2 Numerical analysis for elliptical contact solution

The exact solution for the contact zone requires that the stress or strain distribution under the contact is known. Then, the contact edges are defined at the points where the stresses or strains in the loading direction are zero. For transversely isotropic materials, the exact contact zone is assumed to be an ellipse. The pressure distribution under contact provides the evaluation of the strain distribution as demonstrated in Equation 18, where x and y are respectively first and second principal directions on the contact surface,[1,10] p is the contact pressure, and b and a are respectively the major and minor semi-axes of the elliptical contact.

$$p(x,y) = p_0\left(1 - \frac{x^2}{a^2} - \frac{y^2}{b^2}\right)^{1/2} \qquad (18)$$

Equation 19[1,10] gives the strain in the loading direction ε_{33}, which relates to the surface displacement in the loading direction u_3 and pressure distribution.

$$u(x,y) = \int \varepsilon(x,y) \qquad (19)$$

Since $u_3(x, y)$ cannot be explicitly found, finite element analysis tools can help solve the strain distribution on the sample surface. After determining the solution for u(x,y), the contour of the strain distribution can be found. The zero-strain point on the x-axis is denoted as $x_{\varepsilon 0}$, and the zero-strain point on the y-axis is $y_{\varepsilon 0}$. Based on the assumption of elliptical contact, Equation 20[1,10] provides the two semi-axes of the contact zone, a and b.

$$a = x_{\varepsilon 0}, b = y_{\varepsilon 0} \quad (20)$$

Equation 21 defines the AR of the contact.

$$AR = \frac{b}{a} \quad (21)$$

2.3 REFERENCES

1. Swanson, S. R. Hertzian contact of orthotropic materials. International Journal of Solids and Structures **41,** 1945–1959 (2004).
2. Lin, D. C., Shreiber, D. I., Dimitriadis, E. K. & Horkay, F. Spherical indentation of soft matter beyond the Hertzian regime: Numerical and experimental validation of hyperelastic models. Biomechanics and Modeling in Mechanobiology **8,** 345–358 (2009).
3. Noël, C. F. O., Charles, I. & Cnrs, S. Extension of the Hertz model for accounting to surface tension in nano- indentation tests of soft materials. Assessment 13–17 (2007).
4. Heris, H. K., Miri, A. K., Tripathy, U., Barthelat, F. & Mongeau, L. Indentation of poroviscoelastic vocal fold tissue using an atomic force microscope. Journal of the mechanical behavior of biomedical materials **28,** 383–92 (2013).
5. Liao, Q., Huang, J., Zhu, T., Xiong, C. & Fang, J. A hybrid model to determine mechanical properties of soft polymers by nanoindentation. Mechanics of Materials **42,**

1043–1047 (2010).

6. Carrillo, F. et al. Nanoindentation of polydimethylsiloxane elastomers: Effect of crosslinking, work of adhesion,and fluid environment on elastic modulus. Journal of Materials Research **21,** 535–537 (2006).

7. Oliver, W. C. & Pharr, G. M. Measurement of hardness and elastic modulus by instrumented indentation: Advances in understanding and refinements to methodology. Journal of Materials Research **19,** 3–20 (2004).

8. Wald, M. J., Considine, J. M. & Turner, K. T. Indentation measurements on soft materials using optical surface deformation measurements. Mechanics of Biological Systems **4,** 41–51 (2014).

9. Tan, T. M. & Sun, C. T. Use of Statical Indentation Laws in the Impact Analysis of Laminated Composite Plates. ASME **52,** (1985).

10. Willis, J. R. HERTZIAN CONTACT OF ANISOTROPIC BODIES. J. Mech. Phys. Solids **14,** 163–176 (1966).

CHAPTER 3: A MULTI-INDENT APPROACH TO DETECT THE SURFACE OF SOFT MATERIALS DURING INDENTATION

3.1 INTRODUCTION

3.1.1 Instrumented indentation

Instrumented indentation is a technique with high force and displacement resolution. It measures the local mechanical properties of a material.[52,50,20] The technique monitors the real-time load and indentation depth of a tip with a well-defined size and geometry, and it uses these data in combination with models to obtain material properties.[4,12] Instrumented indentation enables the differentiation of properties over small regions through the use of probe sizes that range from 10μm to 1mm as well as high force and displacement resolution that is less than 1nN and 1nm, respectively.[4,53,29,54] Soft gels with a modulus ranging from 10kPa to 100kPa have been characterized through instrumented indentation with tip sizes between 100μm and 1mm and conical, spherical, or spherical-shaped tips.[1,4,29,55,56 4,25] The primary obstacle in testing soft materials with instrumented indentation is the detection of the sample surface. This paper addresses this key challenge.

Instrumented indentation has been increasingly recognized as an efficient way to understand the biological process of diseased or damaged tissues, which are typically soft and heterogeneous on a scale of tens to hundreds of micrometers.[4,50] The technique has been applied to tissues such as bone and cartilage.[16,30,57] However, fewer studies have examined softer tissues with moduli less than 1MPa, which is in part due to problems with surface detection.[50,24] Yao et al. have characterized the shear modulus and poroelastic properties of human cervix,[25] Slaboch et al. have typified rat thrombus relaxation behavior with indentation,[28] Chhetri et al. have studied elastic properties of vocal folds,[29] and Gupta et al. have identified porcine cartilage time-independent properties.[30] The rising interest in the characterization of soft and heterogeneous

biological materials has driven demand for a more accurate and reliable approach to measure the mechanical properties of these materials via instrumented indentation. This thesis presents an approach to address the issue of surface detection for the indentation of soft materials.

3.1.2 The surface detection problem for the indentation of soft materials

Several challenges complicate the collection of accurate and repeatable data through instrumented indentation of soft materials. Among them, surface detection is arguably the most crucial.[24,58,47] For soft materials, the preload must be sufficiently large to register contact with the material surface. With too small of a preload, the tip-fluid interaction can trigger false engagement, or false engagement can be triggered before full contact is made. With such large preloads, the indentation test typically starts from a deformed surface, i.e. with the probe at some initial preload-induced indentation depth that is below the undeformed surface. This is especially relevant for systems with a small retraction distance of approximately 150 nm. This initial indentation depth can be on the order of microns. There is currently no non-destructive method to determine the initial depth, and the result is an overestimation of properties such as Young's modulus and shear modulus.[58,47]

Previous studies have suggested tracking the surface deformation with florescent particles as a means to resolve the surface detection problem.[47] However, this method requires specialized equipment, and not all materials can be prepared with fluorescent beads on the surface. Li et al. and Bhushan et al. [37] have proposed surface detection by monitoring the change in stiffness through cyclic loading; however, the theory was developed for rigid plastic materials. This approach is not applicable to viscoelastic and viscoelastic-plastic materials because it does not account for time-dependent behavior.[37] Ebenstein et al. have engaged with surface detection through dynamic testing. High-frequency dynamic testing can result in sample heating, which

can in turn cause softening or even melting.[12] Other studies have not addressed the surface detection problem at all.[52,53,29]

This chapter of the thesis proposes the MIA, which indirectly detects the sample surface by determining the preload-induced initial indentation depth. With this initial indentation, the actual indentation depth is greater than the apparent depth, which is defined as the user-prescribed indentation depth. The underestimation of the actual indentation depth inflates the modulus and affects poroelastic properties. The present work employed instrumented nanoindentation to measure the linear elastic and poroelastic properties of polyacrylamide gels, and it compares results from the MIA to those obtained by the Oliver-Pharr approach.[2] Bulk uniaxial compression test data set the standard for comparison of the Young's modulus and shear modulus to the indentation results.

3.1.3 Overview of the Oliver-Pharr model

The MIA method that this study introduces derives from the popular Oliver-Pharr model.[7] The Oliver-Pharr model has been most widely applied to elastic materials with a Young's modulus greater than 1MPa. It has been less commonly used for materials with a modulus between 50kPa and 1MPa, and even more rarely for softer materials.[4] In order to introduce specific concepts and notation that relate to the MIA, Figure 2, and Equations 1 through 7 provide an overview of the Oliver-Pharr model.

Figures 2A and 2B are schematics of the geometry of indentation and the resultant load-displacement curve during loading and unloading, respectively. During the indentation experiment, the probe continuously indents the material to the maximum load, P_{max}, and maximum indentation depth, h_{max} (Figure 2). The depth over which the indenter is in contact with the material is the contact depth, h_c (Figure 2A).

The distance from the contact separation point to the non-deformed surface of the sample is the "sink-in" depth, which is denoted as h_s (Figure 2). It is expressed in Equation 22,[7] where ε is a constant that depends on the geometry of the indenter and is equal to 0.75 for a spherical probe.[7,4] The sum of the sink-in depth and the contact depth is the maximum depth of the indenter, and Equation 23 defines their relationship.

$$h_s = \varepsilon \frac{P_{max}}{S} \quad (22)$$

$$h_c = h_{max} - \varepsilon \frac{P_{max}}{S} \quad (23)$$

The projected or contact area A of the spherical indenter, which is in contact with the material, depends on the contact depth according to Equation 24, where R is the radius of the spherical indenter tip.[7] The contact area is involved in the calculation of the Young's modulus of the sample, E_s, in Equations 25 through 27.

$$A = \pi\left(2Rh_c - {h_c}^2\right) \quad (24)$$

The slope of the unloading curve evaluated at P_{max} is the contact stiffness S, which is illustrated in Figure 1B and expressed by Equation 25. It is a function of the indentation modulus E* the contact area A and a geometric constant β, which has an approximate value of one for the spherical indenter.[7] The modulus of the sample and that of the indenter are contained within Equation 26 for the effective modulus, where the subscript s refers to the properties of the sample, and i represents those of the indenter. Thus, E_s and E_i are the modulus of the sample and indenter, respectively. Likewise, v_s and v_i are the Poisson's ratio of the sample and the indenter, respectively.

$$S = \beta \frac{2}{\sqrt{\pi}} \sqrt{A}\, E^* \quad (25)$$

$$\frac{1}{E_{eff}} = \frac{1-{v_s}^2}{E_s} + \frac{1-{v_i}^2}{E_i} \quad (26)$$

$$E_{eff} = \frac{E_s}{(1-{v_s}^2)} \quad (27)$$

The indenter that was used for this research was sapphire and had a Young's modulus of 345GPa, while the materials of interest all had a modulus far below 100kPa. Therefore, the second term of Equation 26 is small and negligible, which leaves E_{eff} in the form of Equation 27. Substituting h_c, A, and E_{eff} from Equations 23, 24, and 27, respectively, into Equation 25 yields Equation 7:

$$S = \beta \frac{2}{\sqrt{\pi}} \frac{E_s}{(1-{v_s}^2)} \sqrt{\pi \left(2R\left(h_{max} - \varepsilon \frac{P_{max}}{S}\right) - (h_{max} - \varepsilon \frac{P_{max}}{S})^2\right)} \quad (28)$$

3.2 MULTI-INDENT APPROACH

3.2.1 Theory of the MIA for the Oliver-Pharr model

To introduce the MIA and demonstrate its determination of the Young's modulus, we use the Oliver-Pharr model. Figure 3 depicts the geometry of the indentation with a spherical indenter and notation that are specific to our approach.

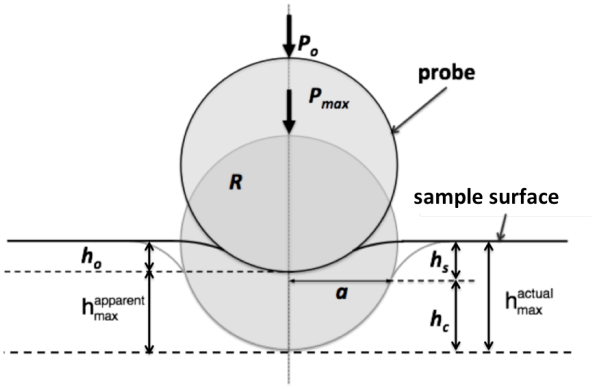

Figure 3. Schematic for the initial indentation depth h_o and its relationship to the actual maximum indentation depth h_{max}^{actual} as well as the apparent maximum indentation depth $h_{max}^{apparent}$

We address the problem of determining the initial indentation depth h_o that results from the preload. If we ignore this initial depth and assume that the indentation begins at the surface of

the sample, then the maximum indentation depth readout from the data, which we call the apparent maximum depth $h_{max}^{apparent}$, is less than the actual depth of the probe in the sample, h_{max}^{actual} (Figure 3). We take this initial indentation depth into account by adding it to the apparent maximum indentation depth as in Equation 8. Substituting h_{max}^{actual} from Equation 29 into Equation 28 yields Equation 30. If the smaller maximum indentation depth $h_{max}^{apparent}$ is used to determine the sample modulus E_s, then it obtains a modulus value that is inflated in relation to the actual sample modulus.

$$h_{max}^{actual} = h_0 + h_{max}^{apparent} \quad (29)$$

$$S = \beta \frac{2}{\sqrt{\pi}} \frac{E_s}{(1-{v_s}^2)} \sqrt{\pi \left(2R \left(h_0 + h_{max}^{apparent} - \varepsilon \frac{P_{max}}{S} \right) - (h_0 + h_{max}^{apparent} - \varepsilon \frac{P_{max}}{S})^2 \right)} \quad (30)$$

We determine h_o by measuring two sequential contact stiffnesses, S_1 and S_2, at the same location, and we assume that the associated initial indentation depth is the same for each. With the two contact stiffnesses, we take the ratio of the squares of S_1 and S_2 and eliminate common terms from Equation 30, including unknowns such as E_s and E_i. Cancelling terms yields Equation 31. The squared terms in the numerator and denominator on the right-hand side of Equation 31 are small for the depths considered here and are therefore neglected. Finally, the initial indentation depth can be determined by solving for h_o as indicated in Equation 32.

$$\frac{S_1^2}{S_2^2} = \frac{\left(h_0 + h_{max1}^{apparent} - \varepsilon \frac{P_{max1}}{S_1} \right) - (h_0 + h_{max1}^{apparent} - \varepsilon \frac{P_{max1}}{S_1})^2}{\left(h_0 + h_{max2}^{apparent} - \varepsilon \frac{P_{max2}}{S_2} \right) - (h_0 + h_{max2}^{apparent} - \varepsilon \frac{P_{max2}}{S_2})^2} \quad (31)$$

$$h_0 = \frac{S_1^2\left(h_{max2}^{apparent} - \varepsilon\frac{P_{max2}}{S_2}\right) - S_2^2\left(h_{max1}^{apparent} - \varepsilon\frac{P_{max1}}{S_1}\right)}{S_2^2 - S_1^2} \quad (32)$$

The two contact stiffnesses S_1 and S_2 are obtained at two different maximum indentation depths, which allows for the determination of h_o and, therefore, the actual indentation depth h_{max}^{actual}. We substitute this value into Equation 30 for either S_1 or S_2, and we determine the Young's modulus of the material from this procedure. This is repeated with the same preload at multiple locations for a homogeneous sample in order to obtain multiple measurements for an average value. Alternatively, for a heterogeneous sample, this is repeated at different preloads in the same location.

3.2.2 Theory of the MIA for Hertzian contact model

The underlying theory of applying the MIA to the Hertzian contact model closely resembles that of applying it to the Oliver-Pharr model. Section 2.1 has described the Hertzian contact theory. With the linear relationship between the maximum indentation force P_{max} and the 1.5 exponent of indentation depth h, the initial indentation depth h_0 can be determined through P_{max1}, P_{max2}, $h_{max1}^{apparent}$, and $h_{max2}^{apparent}$ as $h_0 = \frac{P_{max1}^{2/3} h_{max2}^{apparent} - P_{max2}^{2/3} h_{max1}^{apparent}}{P_{max2}^{2/3} - P_{max1}^{2/3}}$.

3.2.3 Use of the MIA to obtain poroelastic material properties

In many soft materials, including polyacrylamide and other hydrogels as well as biological tissues, poroelasticity has an important role in the material response. Kalcioglu and others have evidenced that the poroelastic response is contact-area dependent.[5,28,29] Therefore, having an accurate value for the contact depth h_c, which is determined from knowing the initial indentation depth h_o, is also significant in determining accurate poroelastic properties. Of particular interest in poroelastic materials are properties such as shear modulus, G, Poisson's ratio, v, diffusivity, D, and intrinsic permeability, κ.

Poroelastic properties are obtained through stress relaxation tests. The shear modulus depends on the maximum load P_{max}, the contact depth h_c, and the radius of the contact depth, a, as defined in Figure 2 and Equation 33. Here, for the spherical indenter, $a = \sqrt{Rh_c}$, and h_c is given by Equation 33.[2] Equation 34 yields h_c after accounting for the initial indentation depth, and Equation 35 calculates P_{max}.

$$P_{max} = \frac{16}{3} G a h_c \quad (33)$$

$$h_c = h_{max}^{actual} - \varepsilon \frac{P_{max}}{S} \quad (34)$$

$$P_{max} = \frac{16}{3} G \sqrt{Rh_c - h_c^2} \left(h_{max}^{actual} - \varepsilon \frac{P_{max}}{S}\right) \quad (35)$$

Poisson's ratio is determined from the ratio of the maximum load, P_{max}, to the relaxed load P_∞ in Equation 36. According to previous studies,[60] diffusivity D is acquired by fitting the normalized force response to Equation 37, given for a spherical indenter, in which $\tau = D/a^2$ is the characteristic relaxation time constant, and P(t) is the load-time response.

$$\frac{P_{max}}{P_\infty} = 2(1 - \nu) \quad (36)$$

$$\frac{P(t) - P_\infty}{P_{max} - P_\infty} = 0.77 \exp\left(-1.92\tau^{0.8}\right) + 0.23 \exp\left(-0.44\tau^{0.52}\right) \quad (37)$$

Finally, the intrinsic permeability κ is found through Equation 38, where η is the viscosity, which is 1.1×10^{-3} Pa.s for the phosphate buffered saline (PBS) used here.

$$k = \frac{D(1 - 2\nu_S)\eta}{2(1 - \nu_S)G} \quad (38)$$

By plotting the normalized force against time normalized by a^2, we can demonstrate whether the material response is dominated by viscoelastic or poroelastic effects. If the normalized force-time curves that are obtained at different maximum indentation depths collapse onto a single curve, then the poroelastic material response dominates over the viscoelastic response.[19]

3.3 EXPERIMENTAL METHODS

3.3.1 Sample preparation for bulk compression and indentation tests

Hydrogels with modulus of 19kPa and 49kPa were made for uniaxial compression and instrumented indentation experiments by preparing polyacrylamide gels according to Poellmann et al.[61] The chemical components for gels of each stiffness were mixed, cast for indentation or compression tests, and finally polymerized for 10 minutes at room temperature. The 19kPa gel contained 58.6wt% DI water, 20% acrylamide stock, and 10% bis stock; the 49kPa gel contained 43.6wt% DI water, 30% acrylamide stock, and 15% bis stock. Both gels also contained 1.2wt% of 10wt% APS and 0.2wt% of TEMED. The ratio of acrylamide stock and bis stock determines the stiffness of the specific gel.[61,62]

3.3.2 Uniaxial compression tests

The Young's modulus as determined by bulk, uniaxial compression tests was used as the standard for comparison to the modulus established through indentation. For bulk samples, the unpolymerized gels were cast into six-well cell culture plates resulting in samples 20mm in diameter and 25mm in height. Compression tests were conducted using a Bose 5100 ElectroForce BioDynamic test system with Bose Wintest control software (TA Instruments, ElectroForce Systems Group, 9625W. 76th street, Suite 15, Eden Prairie, Minnesota). Samples

were tested to 5% strain at a displacement rate of 0.15mm/s, which corresponds to 0.5%/s. A 1,000-g load cell was used. Young's modulus was determined from the linear elastic regime of the stress–strain curve with a custom Matlab code (Matlab, 2014a version, Mathworks, Inc., Natick, Massachusetts). Three samples of each of the two gel formulations were tested in compression, and each individual sample was tested three times for a total of nine measurements for each gel formulation. The calculation of Young's modulus and shear modulus used a Poisson's ratio of 0.33. This value was measured in our previous work.[61]

3.3.3 Indentation tests

For indentation tests, the unpolymerized gel was cast into a 7-cm diameter glass petri dish with a frosted bottom (Figure 4).

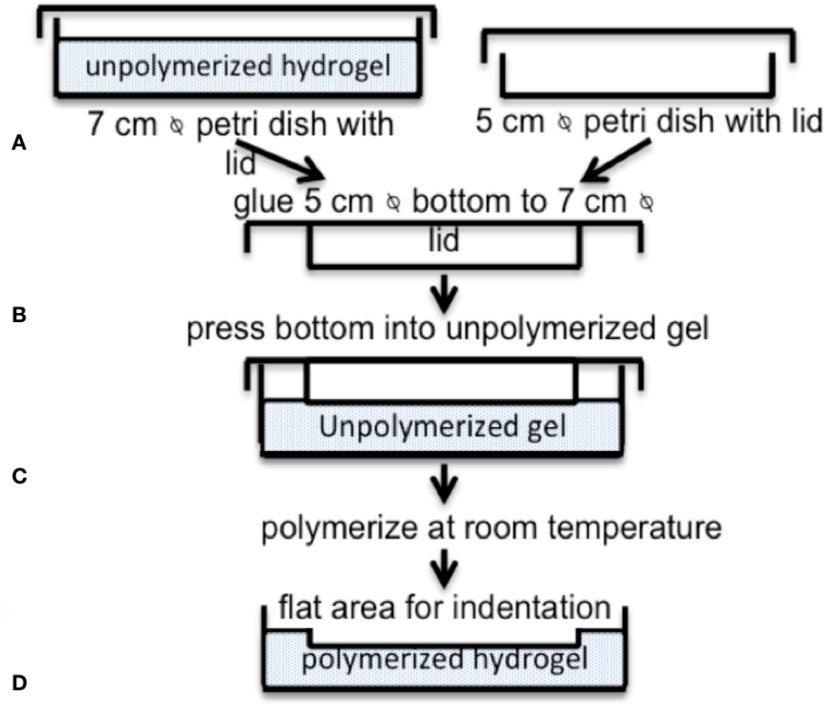

Figure 4. Polyacrylamide gel sample preparation for indentation tests: A. the unpolymerized gel was cast in a 7-cm diameter glass petri dish with a custom-frosted bottom; B. the bottom of a 5-cm diameter petri dish was glued onto the lid of the 7-cm glass petri dish and C. placed onto the surface of the unpolymerized gel; D. a flat surface for indentation tests was obtained during polymerization, and indents were performed on the flat surface that was generated by the procedure

The custom-frosted glass secures the sample in the dish and thus prevents floating and other sample motion during indentation experiments. To generate a flat indentation surface on the gel, the bottom of a 5-cm diameter petri dish was glued onto the lid of a 7-cm petri dish (Figure 4B) and then placed on top of the unpolymerized gel (Figure 4C).

After polymerization, the petri dish was attached to a stainless steel plate and placed on the magnetic platform of the instrumented indentation system (TI950 Triboindenter, Hysitron, Inc., Minneapolis, Minnesota). The force on the indenter probe from the interaction with the fluid was subtracted from the raw data by performing the recommended baseline "air indent" in the fluid with the indenter tip fully submerged.

3.3.3.1 Determination of preloads and maximum indentation depths

The selection of the preload influences the repeatability of the measurements and the signal-to-noise ratio of load-displacement data. An optimized preload ensures that the tip is fully in contact with the sample surface when the indentation test begins, and the preload exceeds any interaction force between the tip and fluid. The fluid layer also adds to the system drift and contributes to false engagement. However, if the preload is too large, the tip may penetrate the sample such that the contact depth exceeds the radius of the tip. The Oliver-Pharr model and the method introduced in this paper assume that the tip-material contact radius is less than the radius of the tip.

To optimize the preload, we compared data from indentation cycles for preloads of 2μN, 4μN, 8μN, and 10μN and assessed the repeatability of the load-displacement data. The appropriate preloads are likely to depend on both the material stiffness and the indentation

system. Thus, while this study provides some guidelines, this test parameter should be optimized for different indentation systems and experiments.

An optimized maximum indentation depth is also essential to avoid false engagement and increase the signal-to-noise ratio in the data. Therefore, the maximum apparent indentation depths used to measure the two contact stiffnesses S_1 and S_2 needed for Equations 30 through 33 should be optimized. For this work, we performed indents with a range of combinations of preloads and indentation depths. However, this paper presents only the load-displacement data from maximum depths of 2μm, 3μm, and 4μm on a 19-kPa sample with a preload of 8μN in the demonstration of selecting the maximum apparent indentation depth.

3.3.3.2 Determination of Young's modulus with multi-indent test procedure

After establishing the preload and maximum apparent indentation depths, two samples for each of the two gels with nominal stiffness 19kPa and 49kPa were tested with the MIA. For each gel, measurements were performed at five independent locations, or spots, at least 1cm apart. To obtain a single measurement for the modulus, a two-indent cycle was performed at the optimized preload to the two established maximum apparent indentation depths. The load/unload displacement rate was 0.2μm/s with a 40-second hold between the two-indent cycles. After the first two-indent cycle, the probe was manually retracted until it was visibly disengaged from the sample surface and then was moved to a new spot for the next two-indent cycle. Each of the two-indent cycles produces one measure of the modulus according to Equations 30 through 33. We report the modulus as an average and standard deviation, which are obtained from averaging the measurements from the two-indent cycles from the five independent spots.

The average modulus resulting from the MIA was compared to that obtained from the bulk uniaxial compression tests and the Oliver-Pharr model, according to Equations 27 and 28,

which does not take into account the initial indentation depth. Statistical significance was established for these three groups through a one-way analysis of variance (ANOVA) followed by a post-hoc Tukey test with $p<0.05$ considered significant (Matlab, 2014a version, Mathworks, Inc., Natick, Massachusetts).

This study used homogenous polyacrylamide gels, and each spot therefore had the same modulus. For heterogeneous materials, such as tissues, the modulus will, by definition, change with the location on the sample. Therefore, a slightly different procedure should be used for heterogeneous materials. Instead of moving to a new spot to repeat the two-indent cycle, the two-indent cycle is repeated at the same spot with two separate preloads in order to perform two measurements of the modulus. To validate this approach, we compared the results obtained at each of the two preloads at five spots on our homogeneous samples. We also compared the results obtained at two preloads to the results acquired from the measurements using a single preload at multiple spots as well as to the bulk compression test measurements. We used 4μN and 8μN for the two final preloads.

3.3.3.3 Multi-indent test procedure for determining poroelastic material properties

Poroelastic properties were determined from load-relaxation data from the hydrogel samples that were prepared for the indentation tests. Relaxation tests were performed in two continuous cycles to two maximum apparent indentation depths, 3μm and 4μm, at the same spot, and the procedure was repeated for a total of five independent spots. Previous studies have illustrated the effect of loading rate and indentation depth on the relaxation curve.[1,30] The relaxation tests in the present study employed the same loading rate for all load-relaxation-unload cycles in order to avoid any differences due to the rate. Samples were loaded at a displacement rate of 2μm/s. For each depth, load-relaxation data were acquired for 40s with a

sampling rate of 200Hz. Data were processed as described in Equations 33 through 38 to determine the instantaneous shear modulus G, Poisson's ratio v, diffusivity D, and permeability k.

The shear modulus was also calculated from bulk measurements, the Oliver-Pharr model, and the MIA. For the bulk value, the shear modulus was obtained using the Young's modulus from the compression tests and the Poisson's ratio from our previous work[61] according to $G = \frac{E}{2(1+v)}$. The shear modulus using the Oliver-Pharr model was determined from Equation 33 with an h_c that was not corrected to account for the initial indentation depth. Finally, the shear modulus was calculated with the h_c determined by the MIA, which accounts for the initial indentation depth (Equations 34-35). The shear modulus was calculated at both 3μm and 4μm for the Oliver-Pharr model and the MIA. The modulus at these two indentation depths was compared via a t-test at $p<0.05$. The data were then combined, and the shear moduli from the three groups were compared in a one-way ANOVA followed by a Tukey test with $p<0.05$ considered significant, as was done for the Young's modulus.

The Poisson's ratio determined by the relaxation experiments was calculated with Equation 36 at the two indentation depths and for five spots. Subsequently, it was compared to the value obtained from the compression test using a t-test with a significance of $p<0.05$. Diffusivity was determined by fitting Equation 37 to the data and determining D from $\tau = D/a^2$. Finally, permeability was calculated with Equation 38. The above procedure yields average values and their standard deviations for at least five independent measurements.

3.4 RESULTS

3.4.1 Determination of preloads and maximum indentation depths

Figure 5 presents the load-displacement data up to maximum apparent indentation depths of 3µm and 4µm on the 19-kPa gel for the 2µN, 4µN, and 8µN preloads. The 2-µN preload was too small; there was frequent false engagement (not represented) due to tip interaction with the fluid layer and low repeatability from spot to spot (Figure 5A). The repeatability of the indentation cycles improved for a 4µN preload (Fig. 5B) and was best for the 8µN preload (Figure 5C). Data from the 10-µN preload were less repeatable compared to those for the 4-µN and 8-µN preloads (not depicted).

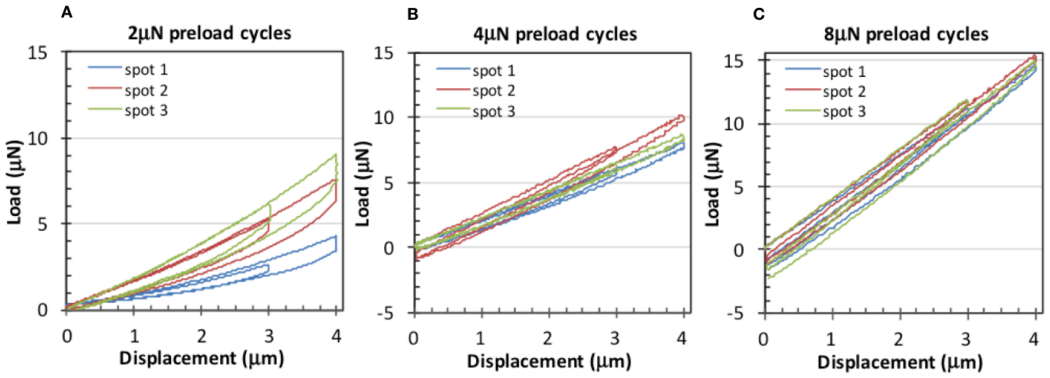

Figure 5. Load-displacement data illustrating preload selection: A. two-cycle load-displacement data for three spots at the 2-µN preload were inconsistent across spots, and false engagement occurred frequently (not depicted); B. Data for cycles at the 4µN preload were more consistent across spots, and false engagement rarely occurred; C. Data for the 8-µN preload were most consistent out of those tested. The preload was determined from a 19-kPa gel that was indented to maximum apparent depths of 3µm and 4µm.

Figure 6 presents load-displacement data from indentation cycles at apparent depths of 1µm, 2µm, 3µm, and 4µm. Data are particularly noisy for the 1-µm depth. Data are most consistent and repeatable and contain the fewest incidences of false engagement for the apparent depths of 3µm and 4µm.

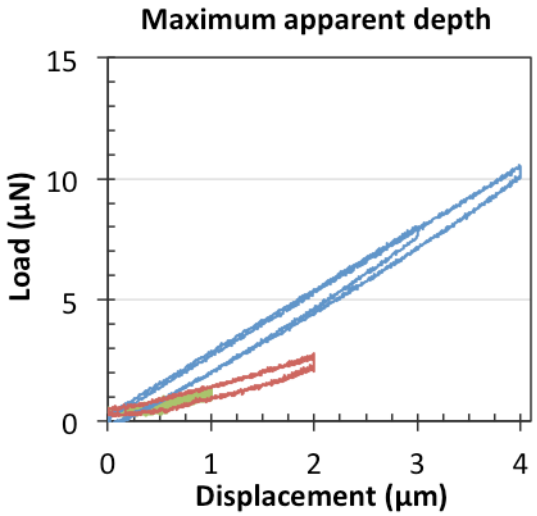

Figure 6. Load-displacement data illustrating the selection of appropriate maximum apparent indentation depths: data are represented for 1µm, 2µm, 3µm, and 4µm for the 19-kPa gel and an 8-µN preload; data for 3µm and 4µm were most consistent and repeatable and contained the fewest incidences of false engagement.

In summary, for the calculation of Young's modulus for a homogeneous material, the optimized preload was 8µN, and the two maximum apparent indentation depths were 3µm and 4µm, respectively. The demonstration to simulate the testing of a heterogeneous material required two preloads and used a 4µN and 8µN preload with these same maximum apparent indentation depths.

3.4.2 Use of the MIA to determine the Young's modulus

To demonstrate the validity of the MIA for determining Young's modulus, we compared the bulk uniaxial compression test results to those obtained with the MIA as well as the Oliver-Pharr model (Figure 7). It is important to note that there was no statistically significant difference between the bulk compression test results and those obtained by the MIA ($p<0.05$). In contrast, the results obtained by the Oliver-Pharr approach, which does not take the initial indentation depth into account, clearly overestimate the modulus, and the overestimation is greater for the softer gel. The average modulus from the compression tests on the 19-kPa and 49-kPa gel

formulations are 17.87±1.14kPa and 48.17±1.03kPa, respectively. Using the MIA, they are 19.87±1.92kPa and 48.23±1.64kPa, respectively. With the Oliver-Pharr model, they are 48.23±3.96kPa and 65.79±4.68kPa, respectively.

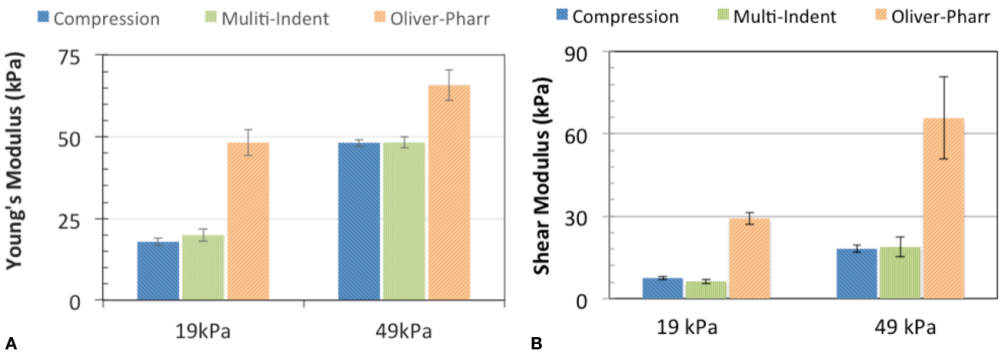

Figure 7. Comparison of A. Young's moduli obtained through the three described methods: a bulk, uniaxial compression test; the MIA; and the Oliver-Pharr model, which does not take the initial indentation depth into account. There is no significant difference between the results obtained from bulk compression tests and the MIA ($p<0.05$). The Oliver-Pharr model grossly overestimated the modulus. B. Shear modulus obtained using the three methods described: bulk, uniaxial compression test; the MIA; and the Oliver-Pharr model. There is no significant difference between the results obtained from bulk compression tests and the MIA ($p<0.05$). The Oliver-Pharr model grossly overestimated the modulus.

To illustrate the use of the MIA to obtain the Young's modulus for a simulated heterogeneous material, we also performed two-cycle indents at two preloads, 4μN and 8μN, on the 19-kPa gel. We compared results to those obtained by compression tests and one single preload. Table 1 indicates that results are consistent at both preloads. The average values obtained over the five spots are 19.33±2.26 and 18.82±2.13 for the 4μN versus 8μN preloads, respectively.

There is no significant difference between results at the two preloads ($p=0.024$), which indicates that both preloads yield valid results. We note that the third spot out of the five has a larger difference between the two preloads. Had this been a new material with unknown properties, we would recommend repeating that measurement to ensure it was not an anomaly or

increasing the number of repeat indents at that spot. Without this datum, the p-value decreases ($p=0.0087$). The average modulus across the two preloads is 19.08±1.98kPa. There is no significant difference between the modulus obtained with two preloads versus the bulk compression test results or the results from MIA in Figure 7.

Table 1. Application of the MIA to a simulated heterogeneous material: indent cycles were conducted at the two preloads for each spot, and there was no significant difference between the modulus obtained at the two preloads ($p<0.05$)

Young's modulus (kPa)			
Indent location	4-μN preload (kPa)	8-μN preload (kPa)	%error
Spot 1	22.07	22.3	1.0
Spot 2	17.92	18.23	1.7
Spot 3	21.05	17.12	18.7
Spot 4	16.51	17.2	4.2
Spot 5	19.12	19.27	0.8
mean±STD	19.33±2.26	18.82±2.13	

3.4.3 Use of the MIA to obtain poroelastic material properties

The MIA was also used to determine poroelastic properties, such as instantaneous shear modulus, Poisson's ratio, diffusivity, and permeability. To demonstrate the use of MIA for the shear modulus, we again compared bulk measurements to those obtained by the Oliver-Pharr model and MIA and using Equations 33 and 35, respectively. Shear modulus was calculated as described. For MIA and the Oliver-Pharr model, shear modulus was calculated at both 3μm and 4μm, and the values obtained at the two depths were compared. There was no statistically

significant difference for either approach at the two depths ($p<0.05$), and the average over the two depths was therefore referenced for any remaining calculations or comparisons. For the MIA, the averages are 6.28±0.86kPa and 18.8±3.56kPa for the 19-kPa and 49-kPa gels, respectively. These averages are 7.47±0.67kPa and 18.13±1.24kPa, respectively, for the bulk measurements, and 29.22±2.18kPa and 65.78±15kPa, respectively, for the Oliver-Pharr model. Figure 8 compares the shear modulus obtained from each approach. There is no significant difference between the MIA and the bulk tests. The Oliver-Pharr approach yields a shear modulus that is significantly greater than those acquired through bulk tests or the MIA.

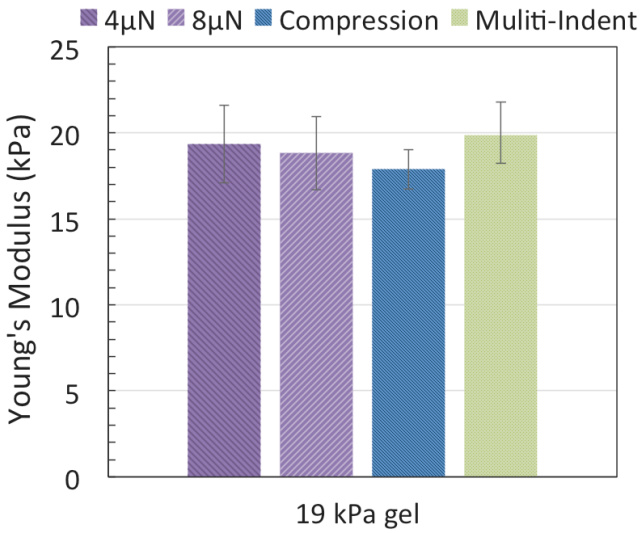

Figure 8. Comparison among tests results of 4-μN preload, 8-μN preload, compression tests, and MIA across spots.

Poisson's ratio was calculated using Equation 36 at 3μm and 4μm, and Table 2 reports the value for the two gels. The value for the 49kPa is highly similar to the experimentally obtained value of 0.35±0.21 versus 0.33 that was noted in previous work for both 19-kPa and 49-kPa gels.[62] The value at 19kPa is 0.427±0.12.

Table 2. Poroelastic properties of 19-kPa and 49-kPa polyacrylamide gel formulations at 4-μm nominal indentation depth

	N	Shear Modulus (kPa)	Poisson's Ratio	Diffusivity(10^{-9}m^2/s)	Permeability (10^{-18}m^2)
49kPa	5	6.28±0.14	0.427±0.03	1.67±0.45	1.16±0.1
19kPa	5	18.8±0.23	0.33±0.025	1.78±0.49	0.87±0.05

We used relaxation curves from the 3-μm and 4-μm depth two-indent cycles to obtain diffusivity and permeability for the gels (Figure 9A and 9C). As previously described, diffusivity was determined by fitting relaxation curves to Equation 37. Figure 9B and 9D contain these data. The values for diffusivity of the 19-kPa and 49-kPa gels are 1.45±0.52 and 1.50±0.43 10^{-9} m^2/s, respectively. Diffusivity was not significantly different for the two gels. Whether the poroelastic or viscoelastic response dominates the material behavior could be determined by whether the normalized curves collapse onto one single curve, which is indeed the case (Figure 8B and 8D). This indicates that the poroelastic relaxation dominates. Finally, the permeability of each gel was determined with Equation 38 and was 1.16±0.13 10^{-18} m^2 and 0.87±0.15 10^{-18} m^2 for the 19-kPa and 49-kPa gels, respectively.

3.5 DISCUSSION

This study presents and validates the MIA as a novel approach to indirect surface detection for instrumented indentation of soft materials. More precisely, the MIA determines the pre-load induced deformation, or the initial indentation depth below the undeformed sample surface. The MIA uses multiple indents at predetermined and optimized preloads and apparent indentation depths to identify this initial indentation depth. Gels with a stiffness of 19kPa and

49kPa were tested using indentation, and elastic properties were compared to those measured by bulk, uniaxial compression tests. Results reflect no difference between results from the MIA versus from bulk compression tests, while results from the Oliver-Pharr model were inflated. Poroelastic properties were also measured. Results notably evidence that the error between the traditional Oliver-Pharr approach and the MIA increased as gel stiffness decreased.

In order to successfully apply the MIA, two parameters require careful selection, namely the preload and the maximum apparent indentation depth. In general, a preload that is too small can cause false engagement, which invalidates the test. Meanwhile, a preload that is too large for any indentation system may introduce an indentation depth that exceeds the maximum radius of the indenter tip. We compared preloads at 2μN, 4μN, and 8μN (Figure 5) and found that the load-displacement data were more repeatable as the preload increased. Thus, we established that both 4μN and 8μN could serve as preloads.

It is important to highlight that other papers on the indentation of soft materials have not reported preload[20,53] despite its significance to the final result. Knowing the preload is particularly crucial for systems in which the retraction distance is less than the preload-induced initial indentation depth. The present research uses a commonly employed system with a retraction distance of 150nm. We note that retraction distance is another testing parameter that has not typically been reported. A larger preload corresponds to a greater initial indentation depth and the less accuracy in the calculation of properties due to the mismatch between apparent and actual maximum indentation depths.

The choice of the maximum apparent indentation depth is similarly important for the final results. An overly small depth also causes false engagement and can result in less repeatable results. We compared load-displacement data for maximum depths of 1μm through 4μm for the

19-kPa gel at an 8-μN preload. Data for 3μm and 4μm were most consistent and had the fewest incidences of false engagement. Thus, these measurements were designated as the maximum apparent indentation depths.

Maximum apparent indentation depths in previous studies have been tens of micrometers.[25,24,63] While these studies have utilized the same probe geometry and a similar tip size as the present study, they have also used a custom indentation system with different constraints. It is important to note that the maximum travel distance during indentation for the system in the present research is only 5μm. This depth is not usually considered a sufficient depth for testing soft materials with an indenter radius of 100μm. However, we successfully indented soft gels and obtained accurate material properties using both a low preload and a small maximum indentation depth. Thus, the MIA can enable the use of some commercial indenters for soft materials whose vertical travel distance is on the order of the maximum indentation depth.

Figure 6 reveals that the MIA results are clearly accurate relative to the standard, while the Oliver-Pharr approach resulted in 150% and 34% overestimations of the Young's modulus for the 19-kPa and the 49-kPa gels, respectively. In view of this, the MIA offers an accurate alternative that is based on the Oliver-Pharr model. Other researchers have studied polyacrylamide gels with indentation. For example, Buffinton et al. have measured the Young's modulus of polyacrylamide gels with moduli ranging from 11kPa to 44kPa using a large, 1-mm diameter conical-spherical tip. Their results agreed with results obtained by bulk compression tests for this large probe.[56]

This study also successfully applied the MIA to determine poroelastic properties of the gels through relaxation tests. In general, the relaxation curve contains information on both viscoelastic and poroelastic effects of the material behavior. If poroelastic effects dominate, the

relaxation curves for various indentation depths should collapse when $\frac{P(t)-P_\infty}{P_{max}-P_\infty}$ and D/a^2 normalize load and time, respectively. In our analysis, if the MIA was not applied, the two normalized relaxation curves did not collapse (Figure 9C and 9G).

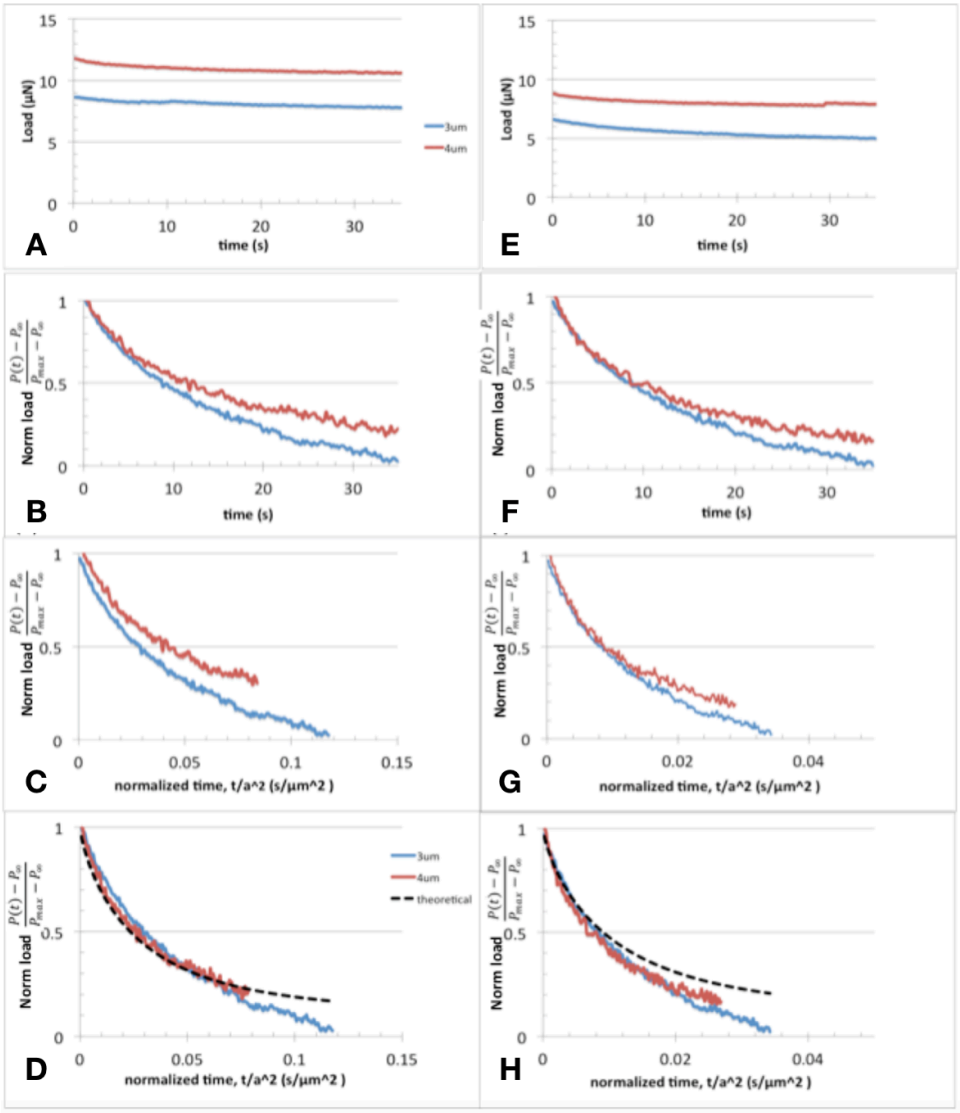

Figure 9. (A-D) Relaxation curves at maximum apparent indentation depths of 3μm and 4μm according to Equation 13 for the 19-kPa gel; (E-H) the 49-kPa gel; (A, D) raw load-time data reflect indentation at two maximum apparent depths; (B, E) normalized load-time data do not overlap; (C, F) normalized load versus normalized time (t/a2) data collapse to one curve, which indicates the dominance of the poroelastic response in the relaxation behavior of the gel.

Conversely, if it was applied, the two curves did indeed collapse. After such collapse was demonstrated, we employed Equations 12 and 15 through 17 to determine shear modulus, diffusivity, and permeability.

The results we obtained for poroelastic properties for our 19-kPa gel are consistent with previous results, although there is not a standard with which to compare diffusivity and permeability. The diffusivity of a 20-kPa gel is 1.6±0.15 x 10^{-10} m^2/s at a 4-μm indentation depth,[4] while we obtained 1.78±0.49 10^{-10} m^2/s for the 19-kPa gel, which was made according to a similar recipe. In previous work, the permeability was 4.2±0.51 x 10^{-18} m^2.[4] By comparison, we obtained 4.87±0.05x10^{-18} m^2. The Poisson's ratio ranged from 0.37±0.005 to 0.41±0.01 in other work.[4,19] With the MIA, we calculated a Poisson's ratio of 0.326±0.025 for the same gel stiffness, and our measurement of 0.33 from bulk tests in our previous work agrees well.[61]

The proposed MIA has several limitations. For example, the MIA is based on the Oliver Pharr model, which does not consider adhesion and friction between the indenter tip and sample surface. However, models that do account for adhesion and friction also rely on knowledge of the contact area as a function of depth. Therefore, application of the MIA can also be extended to more complex models of indentation, such as the Johnson-Kendall-Roberts (JKR)[64] and the Deriaguin-Muller-Toporov (DMT)[65] models. Obtaining accurate results for samples at 10kPa poses additional challenges. Testing gels of such softness is significantly more challenging and requires more attention in order to yield results that are as accurate as those presented here. Thus, caution is necessary when broadly applying the MIA to materials in this range, as researchers should be aware that results may be less accurate. Nevertheless, the use of the MIA results in substantially more accurate results than current commercial indenters can provide. Finally, the MIA has only been validated with homogeneous gels with known properties and linear elastic

behavior. We simulated heterogeneous samples and illustrated that the approach is successful with samples of known properties. The next step is in our research with the MIA is to apply the approach to more complex, heterogeneous materials.

3.6 CONCLUSIONS

The MIA was introduced as an indirect way to detect the sample surface during instrumented indentation of soft materials. The MIA employs data from two apparent indentation depths to determine the depth of the preload-induced indentation; thereby, it indirectly establishes the location of the sample surface. The approach was validated by comparing the results from indentation to results of uniaxial compression tests for 19-kPa and 49-kPa polyacrylamide gels. Results reflect that the MIA yielded significantly more accurate measurements of Young's modulus and instantaneous shear modulus than the standard Oliver-Pharr model can offer, as the latter yielded values inflated by as much as 150% compared to bulk compression tests. The error between results obtained with and without the MIA increased as the stiffness of the gel decreased. Poroelastic properties such as permeability and diffusivity can also be determined more accurately and with small probes and indentation depths. In general, when a large probe is utilized, the relaxation times can be hours versus seconds.[4,53] Results from this study evidence that accurate material properties can be measured with instrumented indentation that uses small preloads and small maximum apparent indentation depths, even when applying probes with a radius as small as 100μm, which requires much shorter relaxation times. The novel approach can alleviate the long-standing challenge of surface detection and enable a more accurate measurement of soft material properties. This advance has the potential to significantly broaden the use of instrumented indentation to test soft materials.

3.7 REFERENCES

1. Oyen, M. L. Analytical techniques for indentation of viscoelastic materials. Philosophical Magazine **86,** 5625–5641 (2006).
2. Oliver, W. C. & Pharr, G. M. Measurement of hardness and elastic modulus by instrumented indentation: Advances in understanding and refinements to methodology. Journal of Materials Research **19,** 3–20 (2004).
3. Vlassak, J. J. & Nix, W. D. Indentation modulus of elastically anisotropic half spaces. Philosophical Magazine A **67,** 1045–1056 (1993).
4. Kalcioglu, Z. I., Mahmoodian, R., Hu, Y., Suo, Z. & Van Vliet, K. J. From macro- to microscale poroelastic characterization of polymeric hydrogels via indentation. Soft Matter **8,** 3393 (2012).
5. McKee, C. T., Last, J. a, Russell, P. & Murphy, C. J. Indentation versus tensile measurements of Young's modulus for soft biological tissues. Tissue engineering. Part B, Reviews **17,** 155–164 (2011).
6. Iivarinen, J. T., Korhonen, R. K. & Jurvelin, J. S. Experimental and numerical analysis of soft tissue stiffness measurement using manual indentation device - significance of indentation geometry and soft tissue thickness. Skin Research and Technology **20,** 347–354 (2014).
7. Hu, Y., Chan, E. P., Vlassak, J. J. & Suo, Z. Poroelastic relaxation indentation of thin layers of gels. Journal of Applied Physics **110,** 13–16 (2011).
8. Chardon, M. K., Rymer, W. Z. & Suresh, N. L. Quantifying the deep tendon reflex using varying tendon indentation depths: Applications to spasticity. IEEE Transactions on Neural Systems and Rehabilitation Engineering **22,** 280–289 (2014).

9. Clayton, J. D. Spherical Indentation in Elastoplastic Materials : Modeling and Simulation. (2005).

10. Genovese, K., Montes, A., Martínez, A. & Evans, S. L. Full-surface deformation measurement of anisotropic tissues under indentation. Medical Engineering and Physics **37,** 484–493 (2015).

11. Kramer, D. E., Volinsky, A. A., Moody, N. R. & Gerberich, W. W. Substrate effects on indentation plastic zone development in thin soft films. Journal of Materials Research **16,** 3150–3157 (2001).

12. Ebenstein, D. M. & Wahl, K. J. A comparison of JKR-based methods to analyze quasi-static and dynamic indentation force curves. Journal of colloid and interface science **298,** 652–62 (2006).

13. Paietta, R. C., Campbell, S. E. & Ferguson, V. L. Influences of spherical tip radius, contact depth, and contact area on nanoindentation properties of bone. Journal of Biomechanics **44,** 285–290 (2011).

14. Spiesz, E. M., Roschger, P. & Zysset, P. K. Elastic anisotropy of uniaxial mineralized collagen fibers measured using two-directional indentation. Effects of hydration state and indentation depth. Journal of the mechanical behavior of biomedical materials **12,** 20–8 (2012).

15. Galli, M. & Oyen, M. L. Fast identification of poroelastic parameters from indentation tests. CMES - Computer Modeling in Engineering and Sciences **48,** 241–269 (2009).

16. Hauch, K. N., Oyen, M. L., Odegard, G. M. & Haut Donahue, T. L. Nanoindentation of the insertional zones of human meniscal attachments into underlying bone. Journal of the mechanical behavior of biomedical materials **2,** 339–47 (2009).

17. Lin, D. C., Shreiber, D. I., Dimitriadis, E. K. & Horkay, F. Spherical indentation of soft matter beyond the Hertzian regime: Numerical and experimental validation of hyperelastic models. Biomechanics and Modeling in Mechanobiology **8,** 345–358 (2009).

18. Wang, Q. M., Mohan, A. C., Oyen, M. L. & Zhao, X. H. Separating viscoelasticity and poroelasticity of gels with different length and time scales. Acta Mechanica Sinica/Lixue Xuebao **30,** 20–27 (2014).

19. Cai, S., Hu, Y., Zhao, X. & Suo, Z. Poroelasticity of a covalently crosslinked alginate hydrogel under compression. Journal of Applied Physics **108,** 1–8 (2010).

20. Heris, H. K., Miri, A. K., Tripathy, U., Barthelat, F. & Mongeau, L. Indentation of poroviscoelastic vocal fold tissue using an atomic force microscope. Journal of the mechanical behavior of biomedical materials **28,** 383–92 (2013).

21. Lake, S. P. & Barocas, V. H. Mechanics and kinematics of soft tissue under indentation are determined by the degree of initial collagen fiber alignment. Journal of the Mechanical Behavior of Biomedical Materials **13,** 25–35 (2012).

22. Bhattacharya, a. K. & Nix, W. D. Finite element simulation of indentation experiments. International Journal of Solids and Structures **24,** 881–891 (1988).

23. Karimzadeh, a., Ayatollahi, M. R. & Alizadeh, M. Finite element simulation of nano-indentation experiment on aluminum 1100. Computational Materials Science **81,** 595–600 (2014).

24. Farine, M. Instrumented Indentation of Soft Materials and Biological Tissues. (2013).

25. Yao, W. et al. Measuring the compressive viscoelastic mechanical properties of human cervical tissue using indentation. Journal of the Mechanical Behavior of Biomedical Materials **34,** 18–26 (2014).

26. Nayar, V. T., Weiland, J. D., Nelson, C. S. & Hodge, A. M. Elastic and viscoelastic characterization of agar. Journal of the mechanical behavior of biomedical materials **7,** 60–8 (2012).

27. Yao, W. et al. Collagen fiber orientation and dispersion in the upper cervix of non-pregnant and pregnant women. PLoS ONE **11,** 1–20 (2016).

28. Slaboch, C. L., Alber, M. S., Rosen, E. D. & Ovaert, T. C. Mechano-rheological properties of the murine thrombus determined via nanoindentation and finite element modeling. Journal of the mechanical behavior of biomedical materials **10,** 75–86 (2012).

29. Chhetri, D. K., Zhang, Z. & Neubauer, J. Measurement of Young's modulus of vocal folds by indentation. Journal of Voice **25,** 1–7 (2011).

30. Gupta, S., Lin, J., Ashby, P. & Pruitt, L. A fiber reinforced poroelastic model of nanoindentation of porcine costal cartilage: a combined experimental and finite element approach. Journal of the mechanical behavior of biomedical materials **2,** 326-37–8 (2009).

31. Bhat, T. S. & Venkatesh, T. A. 3-D Finite Element Analysis of Instrumented Indentation of Transversely Isotropic Materials. Simulia Customer Conference 3–7 (2010).

32. Vanlandingham, M. R. Review of Instrumented Indentation. Journal Of Research Of The National Institute Of Standards And Technology **108,** 249–265 (2003).

33. Lan, H. & Venkatesh, T. a. Determination of the elastic and plastic properties of materials through instrumented indentation with reduced sensitivity. Acta Materialia **55,** 2025–2041 (2007).

34. Calabri, L., Pugno, N., Menozzi, C. & Valeri, S. AFM nanoindentation: tip shape and tip radius of curvature effect on the hardness measurement. Journal of Physics: Condensed Matter **20,** 474208 (2008).

35. Crick, S. L. & Yin, F. C.-P. P. Assessing micromechanical properties of cells with atomic force microscopy: importance of the contact point. Biomechanics and modeling in mechanobiology **6,** 199–210 (2007).

36. Chippada, U., Yurke, B. & Langrana, N. a. Simultaneous determination of Young's modulus, shear modulus, and Poisson's ratio of soft hydrogels. Journal of Materials Research **25,** 545–555 (2010).

37. Li, X. & Bhushan, B. A review of nanoindentation continuous stiffness measurement technique and its applications. Science **48,** 11–36 (2002).

38. Kohn, J. C. & Ebenstein, D. M. Eliminating adhesion errors in nanoindentation of compliant polymers and hydrogels. Journal of the mechanical behavior of biomedical materials **20,** 316–26 (2013).

39. Morrow, D. A., Haut Donahue, T. L., Odegard, G. M. & Kaufman, K. R. Transversely isotropic tensile material properties of skeletal muscle tissue. Journal of the mechanical behavior of biomedical materials **3,** 124–9 (2010).

40. Yin, L. & Elliott, D. M. A biphasic and transversely isotropic mechanical model for tendon: Application to mouse tail fascicles in uniaxial tension. Journal of Biomechanics **37,** 907–916 (2004).

41. Dahan, M. & Zarka, J. Elastic contact between a sphere and a semi infinite transversely isotropic body. International Journal of Solids and Structures **13,** 229–238 (1977).

42. Willis, J. R. HERTZIAN CONTACT OF ANISOTROYIC BODIES. J. Mech. Phys. Solids **14,** 163–176 (1966).

43. Noël, C. F. O., Charles, I. & Cnrs, S. Extension of the Hertz model for accounting to surface tension in nano- indentation tests of soft materials. Assessment 13–17 (2007).

44. Swanson, S. R. Hertzian contact of orthotropic materials. International Journal of Solids and Structures **41,** 1945–1959 (2004).

45. Pareja, N. V. R. Contact and Friction in Systems with Fibre Reinforced Elastomers. Tribology and Surface Technology **PhD,** (2011).

46. Tan, T. M. & Sun, C. T. Use of Statical Indentation Laws in the Impact Analysis of Laminated Composite Plates. ASME **52,** (1985).

47. Wald, M. J., Considine, J. M. & Turner, K. T. Indentation measurements on soft materials using optical surface deformation measurements. Mechanics of Biological Systems **4,** 41–51 (2014).

48. Flynn, C. A model for the anisotropic response of fibrous soft tissues using six discrete fibre bundles Short.

49. Gan, Y. et al. Analyzing three-dimensional ultrastructure of human cervical tissue using optical coherence tomography. Biomedical Optics Express **6,** 1090 (2015).

50. Ebenstein, D. M. & Pruitt, L. a. Nanoindentation of biological materials. Nano Today **1,** 26–33 (2006).

51. Chardon, M. K., Dhaher, Y. Y., Suresh, N. I., Jaramillo, G. & Zev Rymer, W. Estimation of musculotendon kinematics under controlled tendon indentation. Journal of Biomechanics **48,** 3577–3585 (2015).

52. Hu, Y., Zhao, X., Vlassak, J. J. & Suo, Z. Using indentation to characterize the poroelasticity of gels. Applied Physics Letters **96,** 121904 (2010).

53. Galli, M., Fornasiere, E., Cugnoni, J. & Oyen, M. L. Poroviscoelastic characterization of particle-reinforced gelatin gels using indentation and homogenization. Journal of the Mechanical Behavior of Biomedical Materials **4,** 610–617 (2011).

54. fischer Cripps, anthony c. fischer cripps indentation book copy.pdf. (Springer New York).

55. Strange, D. G. T. et al. Separating poroviscoelastic deformation mechanisms in hydrogels. Applied Physics Letters **102,** 3–7 (2013).

56. Buffinton, C. M., Tong, K. J., Blaho, R. A., Buffinton, E. M. & Ebenstein, D. M. Comparison of mechanical testing methods for biomaterials: Pipette aspiration, nanoindentation, and macroscale testing. Journal of the mechanical behavior of biomedical materials **51,** 367–79 (2015).

57. Li, C., Allen, J., Alliston, T. & Pruitt, L. A. The use of polyacrylamide gels for mechanical calibration of cartilage--a combined nanoindentation and unconfined compression study. Journal of the mechanical behavior of biomedical materials **4,** 1540–7 (2011).

58. Kaufman, J. D. & Klapperich, C. M. Surface detection errors cause overestimation of the modulus in nanoindentation on soft materials. Journal of the mechanical behavior of biomedical materials **2,** 312–7 (2009).

59. Hui, C.-Y. & Muralidharan, V. Gel mechanics: a comparison of the theories of Biot and Tanaka, Hocker, and Benedek. The Journal of chemical physics **123,** 154905 (2005).

60. Chan, E. P., Hu, Y., Johnson, P. M., Suo, Z. & Stafford, C. M. Spherical indentation testing of poroelastic relaxations in thin hydrogel layers. Soft Matter **8,** 1492 (2012).

61. Poellmann, M. J. & Wagoner Johnson, A. J. Characterizing and Patterning Polyacrylamide Substrates Functionalized with N-Hydroxysuccinimide. Cellular and Molecular Bioengineering **6,** 299–309 (2013).

62. Poellmann, M. J. & Johnson, A. J. W. Multimaterial polyacrylamide: fabrication with electrohydrodynamic jet printing, applications, and modeling. Biofabrication **6,** 35018

(2014).

63. Hu, Y., Chen, X., Whitesides, G. M., Vlassak, J. J. & Suo, Z. Indentation of polydimethylsiloxane submerged in organic solvents. Journal of Materials Research **26,** 785–795 (2011).

64. Johnson, K. L., Kendall, K. & Roberts, a. D. Surface Energy and the Contact of Elastic Solids. Proceedings of the Royal Society A: Mathematical, Physical and Engineering Sciences **324,** 301–313 (1971).

65. Derjaguin, B. V., Muller, V. M. & Toporov, Y. P. Effect of Contact Deformation on the Adhesion of Particles. Experimental Brain Research **159,** 360–369 (2004).

CHAPTER 4: AN INDENTATION METHOD TO DETERMINE NON-CIRCULAR CONTACT AND ELASTIC MODULI OF TRANSVERSELY ISOTROPIC COLLAGENOUS TISSUE

4.1 INTRODUCTION

Indentation has become increasingly common for characterizing the localized mechanical properties[1–3] of soft materials, including biological tissues. Many of these tissues, including cartilage, tendons, brain, vocal folds, and cervix, are highly anisotropic.[1,4–6] Such anisotropy is evident from the distribution of collagen fibers[7,8] in terms of whether the fibers have preferred alignment directions.[9,10]

Many indentation studies have used a spherical tip for soft tissue, as this type of tip is less likely to penetrate the sample surface compared to a Berkvich tip, which is a three-sided pyramid shape, or a flat punch. Furthermore, a spherical tip can provide a relatively large contact area that enables the use of indentation for especially soft materials, usually below 1MPa in indentation modulus.[6,11,12] Contact theory for isotropic materials assumes that the projected contact area under the spherical tip is circular.[3,13,14] Vlassak and Nix have highlighted that isotropic contact theory is also valid for anisotropic materials as long as the half-plane has three- or four-fold rotational symmetry,[15] like tetrahedral crystals. This assumption by Vlassak and Nix solves the contact problem when fibers distribute without a heavily preferred orientation. However, in many cases, collagen fibers in tissue do have a strong preferred orientation, and the isotropic contact assumption is not valid.[13,15] In previous indentation studies on soft tissue that have utilized a spherical tip, researchers have assumed that the material under the tip is isotropic,[1,5,16,17] and they have made such assumption without examining the local anisotropy.

Studies on contact of anisotropic materials commenced in the 1950s.[13] In 1954, Green and Zerna presented an analytical solution for contact pressure of transversely isotropic

materials;[18] since then, most theories that have been developed or modified have follow from this finding.[19] In 1966, Turner developed a particularly convenient form of the solution that can solve the contact problem if the tensile properties in longitudinal and transverse directions[13,20] are known. The same year, Willis proposed a procedure for determining the strain distribution in the contact region for orthotropic materials. This procedure involves a numerical contour integration[14] and recognizes contact edges from zero-strain boundaries. In 2003, Shi et al. presented a numerical approach for solving the contact problem for orthotropic materials. Their method enables the estimation of the contact stress.[21] The estimation of the location of the zero-contact stress and strain clarifies the contact edges in the contact plane and thus helps evaluate the contact area. An accurate estimate of the contact area is essential to determine the indentation modulus.[13,15]

Some theories assume circular contact for anisotropic materials with modified solutions for the isotropic materials. This study refers to these theories as circular contact approximation. Yang, Tan, and Sun have reported that the contact pressure and area could be obtained from the formulae for isotropic materials, but they used the orthotropic modulus in the loading direction instead of the isotropic indentation modulus.[22,23] Vlassak and Nix have further stated that the isotropic approximation is only valid under low anisotropy, i.e. if the ratio of the longitudinal and transverse modulus is close to one.[15] Swanson has compared the contact area calculated from the exact solution to the circular approximation and also stated that the circular approximation is only valid under low anisotropy on transversely isotropic materials.[13,24]

In elastic contact, the calculation of indentation modulus depends on the evaluation of the contact area.[3,25,26] As previously developed theories demonstrate,[22,23] the circular contact approximation offers a straightforward solution to estimate the contact area in a homogeneous

transversely isotropic material and, therefore, to calculate the reduced indentation modulus. In order to employ this theory, the tensile modulus along and perpendicular to the material symmetry axis requires assessment through uniaxial tensile tests. However, many collagenous tissues are both heterogeneous and anisotropic, and measuring the local tensile moduli in these cases is highly difficult, if not impossible. Therefore, it is a challenge to locally estimate the contact zone for such complex tissues.

The goal of this study is to develop a simple experimental method to determine the indentation modulus of a locally transversely isotropic collagenous material. To validate our approach, we utilized porcine digital flexor tendon, which is a relatively homogeneous transversely isotropic material. However, we also describe how the method can be extended to heterogeneous locally transversely isotropic materials. This paper first explores the relationship between fiber orientation and the AR of contact as well as the relationship between AR and anisotropy level. Next, it examines the relationship between anisotropy level and ratio of contact area (RCA) between the exact solution and isotropic approximation. Lastly, it proposes an experimental method to evaluate the exact value of the indentation modulus of locally transversely isotropic material, which could be conveniently obtained from the circular approximation.

4.2 THEORY

4.2.1 Hertzian contact between a sphere and a half-plane

The contact solution for two deformable and frictionless homogeneous elastic bodies is well developed.[3,13,27] When an elastic sphere of radius R (a spherical indenter in the present

work) indents on an elastic half-space, it has a contact area of radius a. The contact radius relates to the R, and the indentation depth d (Equation 39).[1,13]

$$a = \sqrt{Rd} \quad (39)$$

The force applied to the sample follows Equation 40, where k is a coefficient that relates to R and the indentation modulus E*, which is a modulus related to both the indenter properties E_i and v_i and sample properties E_s and v_s that is expressed in Equations 41 and 42. If the indenter is much stiffer than the sample, E* can be expressed by Equation 43. The exponent q is a shape factor that depends on the shape of the two contact entities. For the elastic contact between a sphere and a half-plane, q = 1.5, and Equation 6 reflects the total contact force.[28] This study employs this form.[3,29]

$$F = kd^q \quad (40)$$

$$k = \frac{4}{3}E^*R^{1/2} \quad (41)$$

$$\frac{1}{E^*} = \frac{1 - v_s^2}{E_s} + \frac{1 - v_i^2}{E_i} \quad (42)$$

$$\frac{1}{E^*} = \frac{1 - v_s^2}{E_s} \quad (43)$$

$$F = \frac{4}{3}E^*R^{1/2}d^{3/2} \quad (44)$$

From Equations 39 through 41, we obtain an expression for the contact radius as a function of the total force, indenter radius, and indentation modulus. Equation 45 presents the final expression of contact radius.

$$a = \sqrt[3]{\frac{3FR}{4E^*}} \quad (45)$$

4.2.2 Transversely isotropic contact theories

4.2.2.1 Circular approximation

Turner presented a general and convenient solution to find the contact radius for transversely isotropic contact problems through formulae that resemble those for isotropic contact problems.[13,20] Equation 46 gives the modulus in Turner's solution, which is the equivalent transversely isotropic modulus E_{equ} instead of the isotropic indentation modulus E^* [13] in Equation 45.[13,22]

$$a = \sqrt[3]{\frac{3FR}{4E_{equ}}} \quad (46)$$

E_{equ} is related to the five material parameters that characterize a transversely isotropic material. E_1 and v_1 are respectively the elastic modulus and Poisson's ratio in the first principal direction x in the contact plane, and E_2 and v_2 are respectively the elastic modulus and Poisson's ratio in the second principal direction y; in this study, $v_1 = v_2 = v$, while G is the shear modulus of the material. Equations 47 and 48 yield E_{equ}.[13,22]

$$E_{equ} = \frac{2}{\alpha\beta} \quad (47)$$

$$\alpha = \left(\frac{E_2/E_1 - v^2}{1 - v^2}\right)^{1/2} \quad \text{and} \quad \beta = \frac{1 + \left(\frac{E_1}{2G} - 1\right) - v(1+v)}{1 - v^2} \quad (48)$$

4.2.2.2 Numerical analysis for elliptical contact solution

The exact solution for the contact zone requires that the stress or strain distribution under the contact is known. Then, the contact edges are defined at the points where the stresses or strains in the loading direction are zero. For transversely isotropic materials, the exact contact

zone is assumed to be an ellipse, and the evaluation of the strain distribution is given by the pressure distribution under contact, as depicted in Equation 49, where x and y are respectively the first and second principal directions on the contact surface.[13,14] Additionally, p is the contact pressure, and b and a are the major and minor semi-axes of the elliptical contact, respectively.

$$p(x,y) = p_0(1 - \frac{x^2}{a^2} - \frac{y^2}{b^2})^{1/2} \quad (49)$$

Strain in the loading direction ε_{33} relates to the surface displacement in the loading direction u_3 and pressure distribution. Equation 50 calculates the strain.[13,14]

$$u(x,y) = \int \varepsilon(x,y) \quad (50)$$

Since we could not explicitly find $u_3(x,y)$, we used finite element analysis tools to help solve the strain distribution on the sample surface. After finding the solution for u (x,y), the contour of strain distribution can be found. The zero-strain point on the x-axis is denoted as $x_{\varepsilon 0}$, and the zero-strain point on y-axis is $y_{\varepsilon 0}$. Based on the assumption of elliptical contact, Equation 51 provides the two semi-axes of the contact zone a and b.[13,14]

$$a = x_{\varepsilon 0}, b = y_{\varepsilon 0} \quad (51)$$

Equation 52 defines the AR of the contact.

$$AR = \frac{b}{a} \quad (52)$$

The RCA is defined as the area calculated with the finite element analysis solution A_{exact} and that calculated by Tuner's approximation for circular contact, A_{circle}.

$$RCA = \frac{A_{exact}}{A_{circle}} \quad (53)$$

This study employs RCA as a correction coefficient, which enables a more accurate estimation of the contact area from the area calculated by circular approximation.

4.3 EXPERIMENTS AND SIMULATIONS

4.3.1 Preparation of isotropic substrates

Polyacrylamide hydrogels with a modulus of 48.23 ± 1.64 kPa were the isotropic substrates. Substrates were prepared according to instructions in a previous study.[30] In brief, they comprised 43.6wt% DI water, 30% acrylamide stock, 15% bis stock, 1.2wt% of 10wt% APS, and 0.2wt% of TEMED. Ten milliliters of the hydrogel solution were mixed in a capped centrifuge tube and subsequently poured into a 3-cm diameter petri dish. The hydrogel solution polymerized over 5 to 10 minutes prior to testing.

4.3.2 Preparation of transversely isotropic substrates

Porcine digital flexor tendons provided the transversely isotropic substrates. Tendons were dissected from frozen pig feet that were obtained from a local grocer the day before the experiments. Prior to the dissection, the feet were thawed at 4°C for 8 hours. All samples were prepared from the segment of the porcine digital flexor tendon as illustrated in Figure 10A.[31]

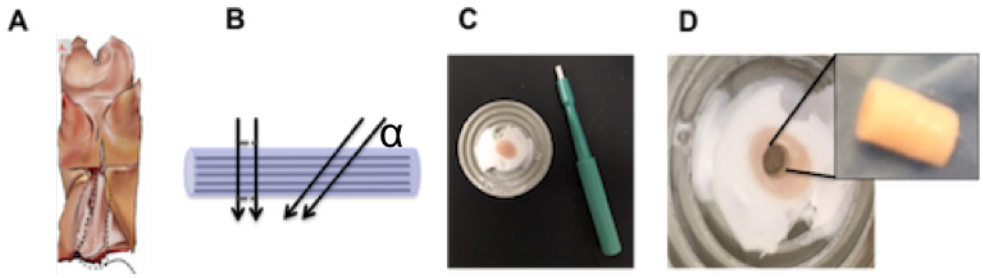

Figure 10. (A) a porcine foot and the location of the porcine digital flexor tendon; (B) the cutting angle of the tendon tissue; (C) a frozen tissue embedded in the OCT compound and a 3.5-mm diameter biopsy punch; (D) a cylindrical tissue that was punched out by the biopsy punch

The flexor tendon with a circular cross-section was first transversely cut into roughly 4-mm sections or at 30°, 45°, or 60° angles with respect to the length of the tendon. The angles were measured with a standard protractor. Figure 10B defines the cutting directions relative to the long axis of the tendon, the fiber orientation, and the cutting angle α. Cryostat sectioning was applied (Leica CM3050 S Research Cryostat, Leica Bio-systems, Nussloch, Germany) to prepare the flat surfaces. Samples were embedded in OCT compound (Tissue-Tek, Sakura Finetek USA, Inc., Torrance, California) and frozen at -20C prior to sectioning, as Figure 10C indicates. The remaining OCT compound was washed away with distilled water. Samples for tensile tests were further prepared in cylinders by 3.5-mm diameter biopsy punch, as Figure 10D demonstrates. The cylindrical shape of the sample minimizes the inaccuracy that results from a non-uniform cross-sectional area and eliminates the constraints from the sheath layer of the tendon tissue. The samples were stored in PBS until testing.

4.3.3 Validation of the linear elastic assumption at low strain

Previous studies have usually assumed tendon to be a transversely isotropic, linear elastic material, as the collagen fibers are densely packed and strongly aligned in the tissue. Turner's solution can relate the tensile modulus to the indentation modulus for a variety of fiber orientations. In order to validate this assumption, we used a two-spring elastic model. We assumed that the matrix is an isotropic, linear elastic material, and the collagen fibers act as unidirectional, linear elastic springs that only take the load in tension. Under this assumption, the whole system was represented as a two-spring system. Figure 11 illustrates a schematic of the two-spring system, wherein the angle θ is the angle between the fibers and the tensile loading direction.

Equation 54 expresses the equivalent tensile modulus $E_{tensile}$ as obtained by tensile tests. As Figure 11 indicates, the matrix modulus E_m is measured as $E_{tensile}$ at θ=90, and the fiber modulus E_f is calculated from Equation 15, with $E_{tensile}$ measured at θ=0. With the knowledge of E_m and E_f, the equivalent tensile modulus $E_{tensile}$ is calculated for fiber orientations between 0° and 90°.

Figure 11 also illustrates the two moduli, E_1 and E_2, along two principal directions in the indentation plane. The indentation angle, ϕ, is defined as the angle between fiber orientation and indentation loading orientation. Directions of E_1 and E_2 are defined in the top views in Figure 11, E1 equals to $E_{tensile}$, and E_2 equals to E_{matrix}, thus, E1/E2 at each Φ (Φ = 90- θ) can be calculated. With knowledge of the relationship between AR and E1/E2 from an FEA simulation, and E1/E2 and Φ, we can obtain the relationship between AR and Φ.

$$E_{tensile} = E_f * \cos\theta + E_m \quad (54)$$

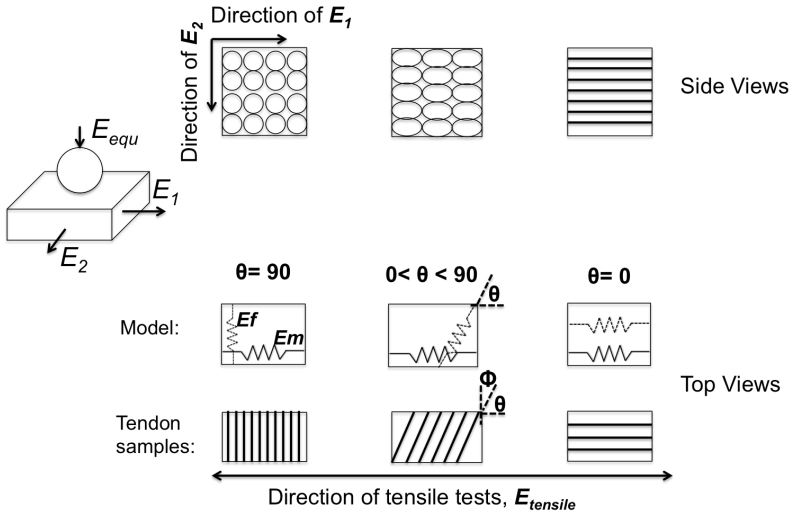

Figure 11. Schematic definition of fiber angles θ for the uniaxial tensile test and Φ for the indentation test as well as the equivalent tensile modulus $E_{tensile}$, the modulus in two principal directions E_1 and E_2, and the equivalent indentation modulus E_{equ}; this figure also defines the direction of the tensile test.

The uniaxial tensile tests are performed using a Bose Electroforce 5110 system. Tendon samples are loaded at θ= 0°, 30°, 45°, 60°, and 90°. Samples were cut into a 3.5-mm diameter cylinder with the biopsy punch as Section 3.1 has described. The two end faces of the cylindrical samples were glued to the top and bottom of the loading platforms with superglue in order to fix both ends of the sample. At the end of each test, the glued boundaries were examined for detachment. Due to deformation of small strains, no detachment occurred at the sample ends and the loading platforms. All samples in the uniaxial tensile tests were loaded to 5% strain at a strain rate of 1%/s using a displacement-controlled waveform. Three samples were tested (N=3) in each fiber orientation θ.

4.3.4 Imaging the contact zone

Three sizes of millimeter-scale stainless steel balls were utilized as spherical indenter tips to study the contact area and shape for isotropic and transversely isotropic materials in load and displacement-controlled experiments. The weights of the balls were measured with Veritas Analytical Balance (Hogentogler & Co., Columbia, Maryland) and were 4mg, 32mg, and 256mg for the 1-mm, 2-mm, and 4-mm diameter balls, respectively. To measure the contact area and AR, the stainless steel balls were submerged in a solution containing 10wt% fluorescent beads (Fluoro-Max™ 1.0um Green Fluorescent Polymer Microspheres) for 30 seconds and then removed and air-dried for at least one minute. The coated steel balls were then used as stamps to mark the contact area by bringing them into contact with the material surface and allowing the fluorescent beads to transfer to the surface. The fluorescent beads that were transferred to the substrate surface were then imaged with a confocal microscope (Nikon Inverted Microscope Eclipse Ti-E). This method is similar to transfer printing. To prevent movement of the fluorescent beads with fluid flow, which can cause overestimation of the AR and contact size,

the excess water on the sample surface was first removed with a piece of tissue paper before stamping. The ball was gently placed on the surface of the sample and left for at least 30 seconds. Subsequently, it was removed and the surface was imaged.

The stamping process left markers consisting of the fluorescent beads on the sample surface. These markers were analyzed with Image J, and the shapes of the contact were processed and analyzed as oval fitting. With the oval selection tool, eight dots on the edge of the marker were chosen. These dots were selected as the furthest visible fluorescent bead.

The method was first applied to a 49-kPa isotropic polyacrylamide gel[30] for method validation. Experimental, theoretical, and finite element analysis results were compared in order to validate the method of marking contact. The modulus and standard deviation of the gel as determined by our previous study[30] were 48.23 ±1.64kPa. The standard deviation for the weight of the ball can be ±0.5%. The upper bound for the contact radius was calculated from the highest possible ball weight and lowest possible modulus. Likewise, the lower bound of contact radius was calculated with the lowest possible ball weight and highest possible modulus. Theoretical contact radii were calculated with Equation 6 and the elastic modulus of the hydrogel.

Stamping the markers on the transversely isotropic substrates, i.e. the tendon, occurred in both load and displacement control. The load control experiments were performed with manual placement of a steel ball. This approach offered a quick and simple way to estimate the contact and did not require additional special equipment, such as displacement or force-sensing systems. However, the manual placement of the steel ball on the sample sometimes resulted in rolling or slipping of the ball on the sample surface, which can lead to inaccurate measures of AR, contact area, or both. Thus, displacement-controlled experiments were also performed on the tendon

samples in order to check the accuracy of the contact AR and area of contact as well as to provide information on the variation in contact with indentation depth.

For the displacement-controlled experiments, a 2-mm stainless steel ball that was cleaned in ethanol was attached with superglue to a vertical, 1-mm diameter stainless steel rod. The steel rod was clamped to a custom piezo-actuated stage, which can be controlled in x, y, and z. After coating the steel ball with the fluorescent beads as described above, the ball was moved in a toward the sample surface until a steep increase in load was detected, as this indicated successful contact between the ball and the sample surface. The contact area and shape were measured at indentation depths of 200μm and 500μm.

4.3.5 Finite element analysis of contact problems

The exact solution of the transversely isotropic contact problem was solved using finite element analysis with ABAQUS (version 6.14). The transversely isotropic material parameters were input are follows: $E_x = E_1$, $E_z = E_y = E_2, v_{xz} = v_{yz} = v_{xy} = v$, $G_{xz} = G_{yz} = G_{xy} = G = \frac{E_1}{2(1-v)}$. E_1 and E_2 were obtained from uniaxial tensile tests and Poisson's ratio was assumed to be 0.4, which previous studies have reported.[5,32,33] The bottom of the sample was constrained in both displacement and rotation in all directions. Sample edges and the top of the sample were unconstrained. The contact between the tip and the material surface was set as "hard contact," which guaranteed that the tip did not cut through the sample during the simulation. The indenter moved toward the sample surface on the z-axis without rotation. Normal strain in the z-axis was plotted along the x- and y-axes, and the semi-axes of contact a and b and the AR of contact were obtained through Equations 51 and 52.

4.3.6 Analysis Methods

4.3.6.1 Contact analysis for isotropic substrates

The contact analysis of the isotropic substrates validated the experimental method for marking the contact area and the AR of the contact between the steel ball and the substrates. A comparison of the measured contact area and the AR to analytical and numerical results corroborated the experimental findings.

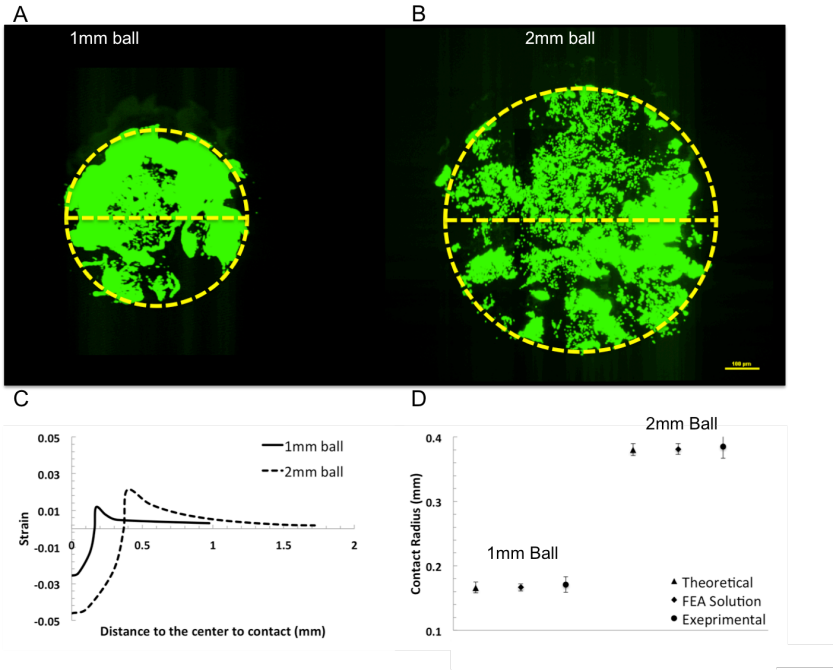

Figure 12. (A, B) Contact marker left by the 1-mm and 2-mm diameter steel balls, respectively; (C) simulation result for 1-mm and 2-mm ball for the isotropic substrate; the plot represents the surface normal strain near the contact zone versus the distance from the contact center; (D) mean values as well as the error range of contact radii from the experiment, the finite element analysis solution, and the analytical solution of the contact problem for the 1-mm and 2-mm diameter ball.

The steel balls with diameters of 1mm and 2mm were used to mark the contact for isotropic substrates. Figure 12A and 12B illustrate representative contact markers on isotropic materials for the two ball sizes, respectively. Figure 12C plots the z-component normal strain,

which was obtained from the finite element analysis as a function of radial distance from the center of the ball. The contact radii were recognized from the radius at which the strain changes from compression to tension, i.e. at zero normal strain. Figure 12D summarizes the results for contact radius from the experiments, the analytical solutions, and the finite element analysis model. The experimental results are expressed as the average ± standard deviation.

4.3.6.2 Contact analysis for transversely isotropic substrates

Some previous studies with indentation[1,2,34] have assumed soft tissues to be linear elastic and directly fit the indentation moduli from load-unload curves without validating the assumption. The present study adapted the theoretical solution for the contact problem for transversely isotropic substrates from that for isotropic linear elastic substrates. We used the two-spring tensile model in combination with the tensile experiments to validate the linear-elastic assumption.

4.4 RESULTS AND DISCUSSION

4.4.1 Results for isotropic substrates

Contact radii from the images in Figure 12A and 12B are 0.174±0.012mm and 0.397±0.021mm, respectively, for the 1-mm and 2-mm balls. The AR of the contact for the isotropic substrate is equal to one, as expected. The contact radii as calculated by Equation 6 are 0.157±0.01mm and 0.376±0.023mm for the 1-mm and 2-mm balls, respectively. The finite element analysis solution yielded 0.163±0.013mm and 0.38±0.02mm for contact radii. The error bars for the two other solutions were obtained by incorporating the average and standard deviation of the Young's modulus for the gel, 48.23 ±1.64kPa, and the variability in the weight of

the steel balls, ±0.5%, as described previously. Error between experimental and analytical is 2.4% for 1-mm ball contact and 1.9% for the 2-mm ball. The average contact radii from the experiments are slightly higher than the radii from the numerical solutions. While a statistical analysis is not appropriate in this case to compare the contact radii that were obtained from the three methods, the two sets of radii as calculated analytically or determined by finite element analysis fall within the standard deviation of the experiments.

Since the stain marker was used for contact zone measurement, the image quality is important. Images in Figure 12A and 12B illustrate that we were able to obtain a clear boundary through the stamping approach. Two critical factors affect the quality of the image: first, the amount of fluid between the ball and the surface of the substrate, and second, the concentration of fluorescent beads. In our experience, the control of the amount of fluid left between the ball and the substrate affects the amount of marker overflow. Specifically, more fluid left between the two entities renders it more likely that the beads will overflow and thus exaggerate the contact marker. Therefore, the balls were dried in air for about one minute, as the methods have noted, and the surface of the substrate was dried in air for two to three minutes prior to stamping. The concentration of the fluorescent beads affects how much we can focus on the contact boundary. If the concentration is too high, the light reflection from marker will be too bright and overestimate contact boundary. Conversely, if the concentration too low, the marker will not be clear or sufficiently continuous for imaging. This study tried multiple concentrations and found that a concentration of 10% was most suitable.

We compared the contact radii between experimental measurements, analytical calculations, and finite element analysis solutions in order to validate if our experimental contact measurements match the contact theory. The contact theory for isotropic substrates is linear

elastic contact theory, and it is valid since we our previous study[30] has proven that the hydrogel in the present study is linear elastic up to at least 4.8% strain, which is the maximum strain that we observed in Figure 12C. The contact theory explains that the contact problem is a compression-tension mixed problem. In Figure 12D, the error caused by the experiment results in around 0.9% error in the modulus calculation in comparison with theoretical and finite element analysis results. This small error indicates that measuring the marker left by the contact between the ball and the substrate is an effective way to characterize the contact.

4.4.2 Results for transversely isotropic substrates

The tensile modulus at $\theta = 90$ is 70kPa; according to Equation 16, this value should be the matrix modulus E_m, which is 70kPa. The tensile modulus at $\theta = 0$ is 66MPa, and with Equation 16 and a known E_m, the fiber modulus E_f was calculated as 67MPa. Figure 4B plots the equivalent tensile modulus $E_{tensile}$, which was calculated between $\theta = 0°$ and 90° from Equation 15 with known E_m and Ef. Figure 4B also plots $E_{tensile}$ from uniaxial tensile results at 30°, 45°, and 60° fiber orientations. The root mean square ($RMS = \frac{1}{n}\sum_1^n(y_{exp}(i) - y_{exp}(i))$) as calculated between experimental and theoretical results at three fiber orientations is 0.48.

From the results in Figure 13B, our measurements agree well with the theoretical curve (RMS=0.48), so the linear-elastic assumption at low strain (5%) is valid for the transversely isotropic material of porcine digital flexor tendon.

Figure 14 summarizes the contact mark imaging results from load- and displacement-controlled experiments. The results together with the statistical analyses reflect that AR depends on orientation but not on steel ball size or indentation depth. The following statistical comparison

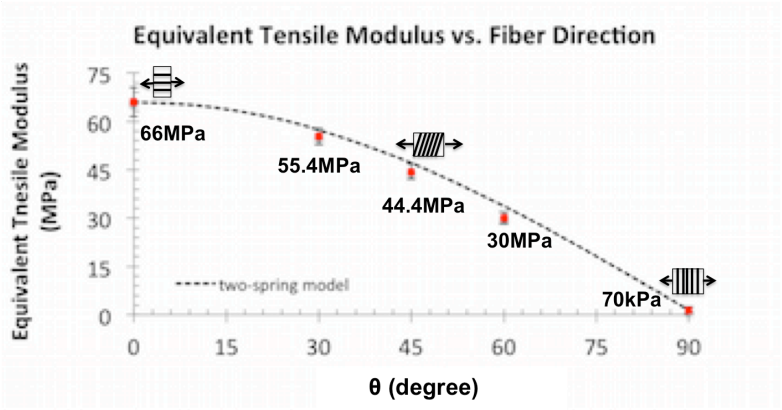

Figure 13. The tensile modulus for the uniaxial tensile tests for the tendon at different θ, depicted as an average +/- standard deviation (symbols); the equivalent tensile modulus $E_{tensile}$ (Equation 15) is plotted for various fiber orientations according to the two-spring model and with 70kPa and 67MPa as the matrix and fiber modulus, respectively

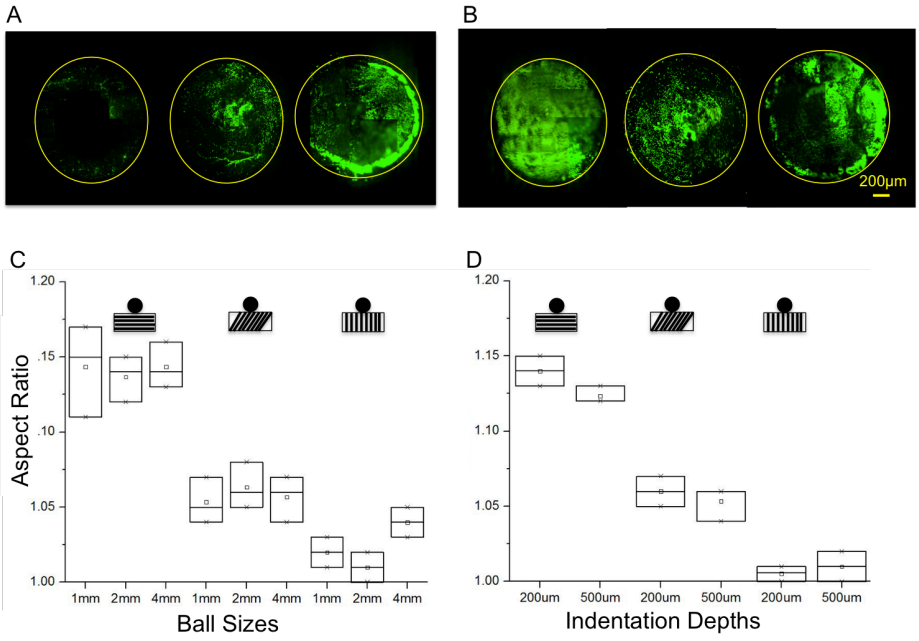

Figure 14. (A, B) Representative images of the contact marker from the load- and displacement-controlled experiments, respectively; (C) box plots of AR for the three steel ball sizes at indentation angles Φ = 0°, 45°, and 90° (N=3); (D) box plots of AR for the 2-mm steel ball at indentation depths of 200 and 500 microns at Φ = 0°, 45°, and 90° (N=5).

were conducted to reach this conclusion. For load control (Figure 14A and 14C), a one-way

ANOVA test was performed on the AR of contact between the results at the same fiber direction but with different ball sizes. No significant difference emerged within any fiber orientation ($P>0.05$). For displacement control (Figure 14B and 14D), a student t-test was performed between results at the same fiber orientation but different indentation depths, and no significant difference was visible within any fiber orientation ($P>0.05$). A one-way ANOVA with a post-hoc Tukey test was further applied for the three fiber orientations in both load and displacement control. The results evidence significant differences in AR between the three orientations ($P<0.05$). The post-hoc Tukey analysis reflects significant differences between the two in each group. Student t-tests were also run at the same fiber orientation but between the load control and displacement control, and they revealed no significant difference in AR ($P<0.05$).

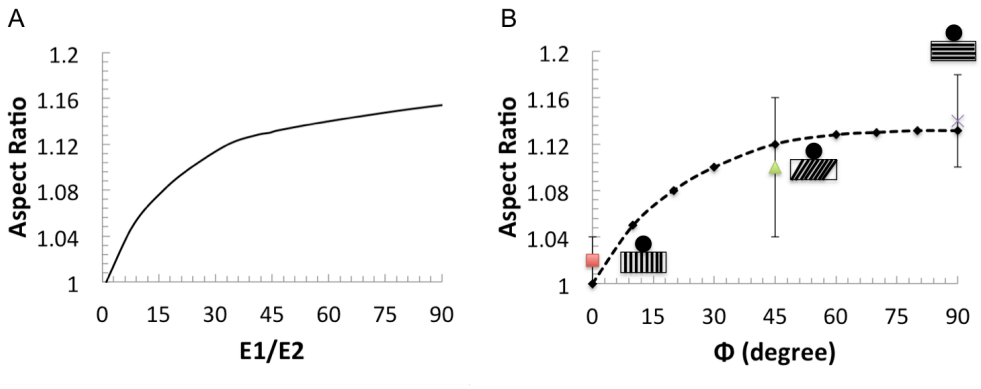

Figure 15. (A) Relationship between AR and the ratio of the E1/E2 as calculated by the finite element analysis solution; Figure 2 defines E1 and E2, which are the moduli in the two principal directions in the contact plane; (B) Comparison of the experimental results of AR as measured at $\Phi = 0°$, 45°, and 90° with those calculated from the finite element analysis solution at various Φ (defined in Figure 2)

Figure 11 defines E1 and E2, and Figure 15A provides the relationship between the AR of contact versus E1/E2. The AR versus Φ was calculated and is plotted in Figure 15B. The experimental results of AR at $\Phi = 0°$, 45°, and 90° were also plotted in Figure 15B for

comparison. The AR at Φ = 0°, 45°, and 90° are respectively 1.02±0.06, 1.09±0.04, and 1.14±0.07. The RMS between the finite element analysis solution and experimental result is 0.22.

Results illustrate that the AR is independent of both indentation load and depth; however, it is not independent of fiber orientation. The statistical analysis also evidences that the measurements of AR from load control and displacement control are not significantly different despite the results from displacement control leading to a smaller standard deviation. This suggests that the simple load control method can be employed as it was in this study to obtain the contact mark, provided no controlled stage is available.

Figure 14 also reflects that a larger angle between the fiber orientation and loading direction of indentation corresponds to a larger AR.

Several previous studies have illustrated this finding,[13,24] and this study further validates it with Figure 15B (RMS=0.22). The AR that was measured with the method in this study is valid. As previously discussed, it is almost impossible to measure the tensile modulus in the two principal directions of the indentation plane (E_1 and E_2) for heterogeneous materials. However, Figure 15A can enable researchers to estimate the ratio of the two local tensile moduli in the indentation plane by simply making an indentation marker at the location of interest and measuring AR, as the axes of the ellipse are expected to align in the principle directions.

Figure 16 compares the contact areas from the experiments to the analytical values and the finite element analysis solutions. Figure 17 gives the relationship between RCA and E1/E2, as obtained from the finite element analysis solution.

Figure 17 contains the results of the measured contact areas. Figure 17A and 17B depict

results from load- and displacement-controlled experiments, respectively. As Chapter 2 has noted, the contact area can be calculated with various assumptions. Poisson's ratios v_x, and v_z are assumed to be 0.4. Shear modulus Figure 16 plots the areas calculated from the Turner's solution, A_{circle}, in dashed lines. In the same figure, solid lines represent the contact areas A_{exact} that

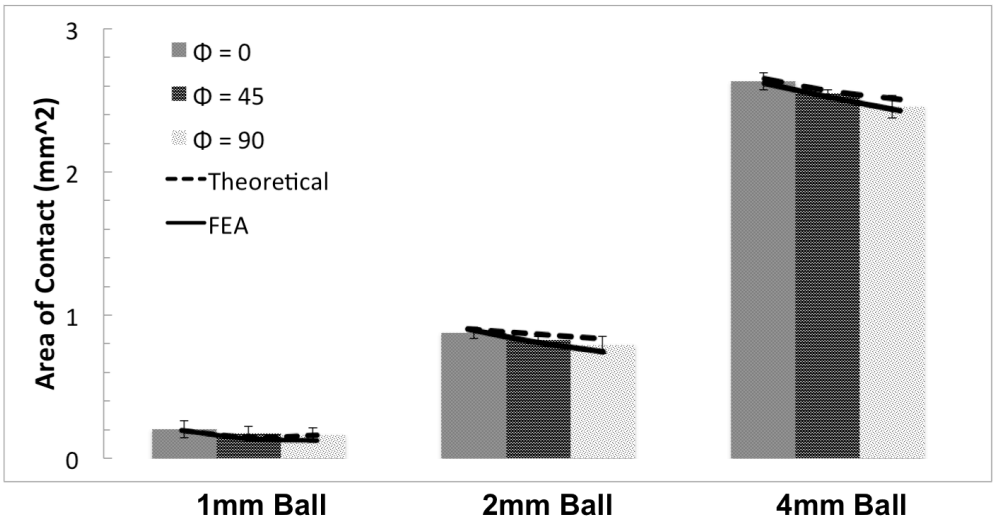

Figure 16. Comparison of measured contact areas with the theoretical values from the circular approximation and finite element analysis solutions.

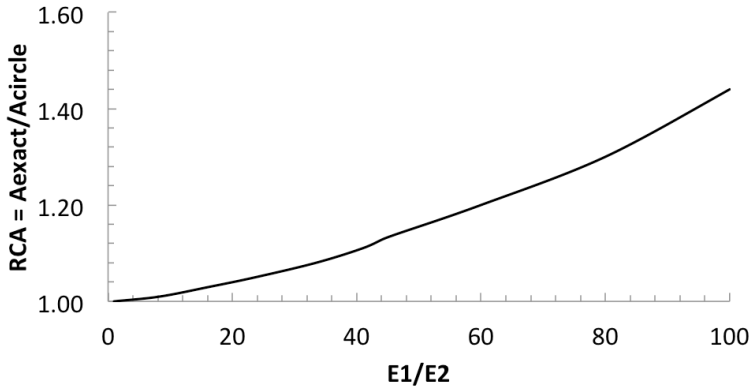

Figure 17. The RCA increases alongside increasing anisotropy in the contact plane

resulted from the finite element analysis solution. Figure 16 also conveys the error

between experimental measurements and Turner's solution and between experiments and finite element analysis solutions. A larger Φ corresponds to a larger the error is between the experiments and Turner's solution. The RCA between the Turner's solution and the finite element analysis solution are plotted at E1/E2 = 0, 20, 40, 60, 80, and 100. Figure 17 gives the RCA versus E1/E2.

The results in Figure 16 reveal that the error between the experimental contact radius A_{exp} and A_{circle} increases when the fiber orientation angle increases. According to Figure 13, we conclude that a larger angle of the fiber orientation coincides with a larger E_1/E_2. Previous studies have also demonstrated and validated that circular approximation is suitable only for low anisotropy.[13,15] Many previous experimental studies on indentation of transversely isotropic or locally transversely isotropic materials[1,4,5] have not examined the non-circular contact area and may thus have introduced large errors into the indentation modulus of interest.

Figure 17 indicates the degree of difference between the circular approximation and the elliptical solution. Since E_1/E_2 is not a value that can be directly measured through experiments, we combined Figure 17 with Figure 15A to clarify the relationship between RCA and AR in Figure 18, which enables a quick estimation of the extent of inaccuracy in the contact area when using circular approximation to calculate indentation modulus.

Figure 15A and Figure 17 established the relationship between RCA and AR, which was plotted in Figure 18, where AR can be directly measured from the contact marker. We indented to different depths with the previously described E_1/E_2 values, and no difference in RCA was found, which reflects that RCA does not relate to the indentation load or depth. Based on Equation 46, Equation 55 expresses the exact solution for the indentation modulus.

$$E_{exact} = E_{circle} * RCA^{-\frac{3}{2}} \quad (55)$$

4.4.3 Discussion on estimating the contact on a heterogeneous, locally transversely isotropic material

As the introduction has stated, the main purpose of this study is to develop a method that equips researchers to quickly estimate the local indentation modulus of a locally transversely isotropic and heterogeneous material. Such a method could yield a more accurate measure of indentation modulus without the need for a complicated analytical solution or tensile tests on the region. Such tests are not being possible for many tissues with small samples that cannot be prepared for mechanical testing. This section we propose steps for applying the method to heterogeneous, locally transversely isotropic materials.

The first step is to characterize the local fiber distribution in the region of interest. Because the method assumes local transversely isotropic symmetry, the regions in which the local fibers are aligned will offer the most accurate results. Techniques like second-harmonic generation (SHG)[35] or optical coherence tomography (OCT)[36] can be effective to study the fiber distributions.

The second step is to choose an appropriate size for the spherical indenter or a ball of known size for stamping, i.e. imaging the contact area and AR. The indenter should be sufficiently smaller than the area of interest so that the strain field does not develop out of the region of interest. The spherical indenter can be coated in accordance with the description in Section 3.4 and subsequently employed as a stamp. Then, the stamped region can be imaged with confocal or fluorescent microscopy.

Next, a marker is made on the sample surface via the contact of a ball, which permits

measurement of the contact area and AR. The RCA is obtained at the measured AR from Figure 18. Indentation modulus E_{circle} is obtained by applying a Hertzian fit to the loading curve of the load-displacement indentation curve. Then, Equation 48 and 54 calculate E_{exact}. Since both AR and RCA are not dependent on the load and depth, the marker can be left at any depth as long as it does not exceed the linear zone of the material, which is typically a maximum of 10% of the tip radius, though this can vary by test material.

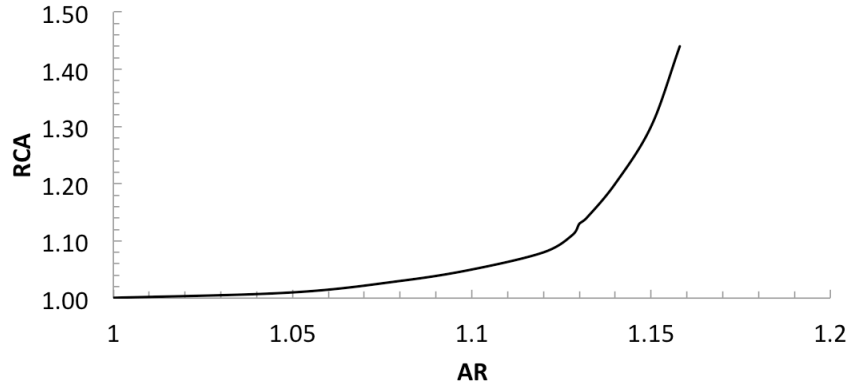

Figure 18. The RCA versus AR

4.5 LIMITATIONS OF THE STUDY

All the theories involved in this study are based on the linear-elastic assumption, and tensile tests were confined by low strain (5%), and can only be applied to materials that are transversely isotropic, or local transversely isotropic (for examples, fiber-reinforced materials with non uni-directional fiber distributions). The method may not be applicable for tensile tests that surpass the linear regime or for highly nonlinear materials. The method also requires a visualization of the indent via the described method or another approach, which can be difficult with small tip sizes. For the demonstrated method, the minimum ball radius with which we could make a visible mark was 500um (Data not shown). No ball smaller than this size could provide a

clear indenter marker using the exact approach described. Furthermore, it may not be possible to coat the tip with the fluorescent beads for certain experimental set ups. In our case, we used a custom system that made it possible to use the stamping technique. However, we could not employ this method with commercial systems in shared facilities. We also found that the experimental results were consistently slightly higher than those obtained by finite element analysis and the analytical solution. This may be caused by adhesion of the tip to the surface or the fluid that carried the fluorescent beads. Nevertheless, we demonstrated that the level of experimental error was not problematic. Since the stamping was not performed in fluid, adhesion effects may have been present. Despite this result, the experimental results were not statistically different from the others. This study also did not consider time-dependent behaviors, such as the viscoelasticity and poroelasticity of the materials. In order to develop a more complete understanding of the tissue, these time-dependent material behaviors warrant investigation with experiments and modeling.

4.6 SUMMARY AND CONCLUSIONS

This study has developed a simple experimental method to determine the indentation modulus of a locally transversely isotropic collagenous material. The staining process in our approach was first validated with an isotropic polyacrylamide gel and later applied to the transversely isotropic tendon tissue. This study concluded that displacement control yields results with higher quality. However, if no controlled stage is available, then the simple load control method can be applied as illustrated here in order to obtain the contact mark.

The experimental, theoretical, and finite element analysis results for AR and the contact areas at various fiber orientations were compared. The study suggests that AR is dependent on neither load nor displacement but is instead related to material properties (anisotropy level). The

relationship between AR and RCA was established at the end of the study, which enabled correction of the indentation modulus as calculated by circular approximation. The research also provided application and experimental steps to utilize the method with heterogeneous, locally transversely isotropic material. These steps can offer guidance to future studies on heterogeneous tissue that use indentation.

4.7 REFERENCES

1. Heris, H. K., Miri, A. K., Tripathy, U., Barthelat, F. & Mongeau, L. Indentation of poroviscoelastic vocal fold tissue using an atomic force microscope. Journal of the mechanical behavior of biomedical materials **28,** 383–92 (2013).
2. Iivarinen, J. T., Korhonen, R. K. & Jurvelin, J. S. Experimental and numerical analysis of soft tissue stiffness measurement using manual indentation device - significance of indentation geometry and soft tissue thickness. Skin Research and Technology **20,** 347–354 (2014).
3. Lin, D. C., Shreiber, D. I., Dimitriadis, E. K. & Horkay, F. Spherical indentation of soft matter beyond the Hertzian regime: Numerical and experimental validation of hyperelastic models. Biomechanics and Modeling in Mechanobiology **8,** 345–358 (2009).
4. Wei, X., Räsänen, T. & Messner, K. Maturation-related compressive properties of rabbit knee articular cartilage and volume fraction of subchondral tissue. Osteoarthritis and Cartilage **6,** 400–409 (1998).
5. Chardon, M. K., Rymer, W. Z. & Suresh, N. L. Quantifying the deep tendon reflex using varying tendon indentation depths: Applications to spasticity. IEEE Transactions on Neural Systems and Rehabilitation Engineering **22,** 280–289 (2014).
6. McKee, C. T., Last, J. a, Russell, P. & Murphy, C. J. Indentation versus tensile

measurements of Young's modulus for soft biological tissues. Tissue engineering. Part B, Reviews **17,** 155–164 (2011).

7. Roeder, B. a, Kokini, K., Sturgis, J. E., Robinson, J. P. & Voytik-Harbin, S. L. Tensile mechanical properties of three-dimensional type I collagen extracellular matrices with varied microstructure. Journal of biomechanical engineering **124,** 214–222 (2002).
8. Thomopoulos, S., Marquez, J. P., Weinberger, B., Birman, V. & Genin, G. M. Collagen fiber orientation at the tendon to bone insertion and its influence on stress concentrations. Journal of Biomechanics **39,** 1842–1851 (2006).
9. Lake, S. P. & Barocas, V. H. Mechanics and kinematics of soft tissue under indentation are determined by the degree of initial collagen fiber alignment. Journal of the Mechanical Behavior of Biomedical Materials **13,** 25–35 (2012).
10. Gasser, T. C., Ogden, R. W. & Holzapfel, G. A. Hyperelastic modelling of arterial layers with distributed collagen fibre orientations. 15–35 (2006). doi:10.1098/rsif.2005.0073
11. Genovese, K., Montes, A., Martínez, A. & Evans, S. L. Full-surface deformation measurement of anisotropic tissues under indentation. Medical Engineering and Physics **37,** 484–493 (2015).
12. Jee, T. & Komvopoulos, K. In vitro measurement of the mechanical properties of skin by nano/microindentation methods. Journal of Biomechanics **47,** 1186–1192 (2014).
13. Swanson, S. R. Hertzian contact of orthotropic materials. International Journal of Solids and Structures **41,** 1945–1959 (2004).
14. Willis, J. R. HERTZIAN CONTACT OF ANISOTROYIC BODIES. J. Mech. Phys. Solids **14,** 163–176 (1966).
15. Vlassak, J. J. & Nix, W. D. Indentation modulus of elastically anisotropic half spaces.

Philosophical Magazine A **67,** 1045–1056 (1993).

16. Seifzadeh, A., Wang, J., Oguamanam, D. C. D. & Papini, M. A nonlinear biphasic fiber-reinforced porohyperviscoelastic model of articular cartilage incorporating fiber reorientation and dispersion. Journal of Biomechanical Engineering **133,** 81004 (2011).
17. Yao, W. et al. Measuring the compressive viscoelastic mechanical properties of human cervical tissue using indentation. Journal of the Mechanical Behavior of Biomedical Materials **34,** 18–26 (2014).
18. Williams, L. N., Elder, S. H., Bouvard, J. L. & Horstemeyer, M. F. The anisotropic compressive mechanical properties of the rabbit patellar tendon. Biorheology **45,** 577–586 (2008).
19. M., C., G., D., M., S. & J.J., V. The general 3D Hertzian Contatc Problem for Anisotropic Materials.
20. Wald, M. J., Considine, J. M. & Turner, K. T. Indentation measurements on soft materials using optical surface deformation measurements. Mechanics of Biological Systems **4,** 41–51 (2014).
21. Shi, Y. & Vesely, I. Fabrication of mitral valve chordae by directed collagen gel shrinkage. Tissue engineering **9,** 1233–1242 (2003).
22. Tan, T. M. & Sun, C. T. Use of Statical Indentation Laws in the Impact Analysis of Laminated Composite Plates. ASME **52,** (1985).
23. Sun, S. H. Y. and C. T. Indentation Law for Composites Laminates. in Composite Materials: Testing and Design, 6th Conference 425–449 (1981).
24. Pareja, N. V. R. Contact and Friction in Systems with Fibre Reinforced Elastomers. Tribology and Surface Technology **PhD,** (2011).

25. Clayton, J. D. Spherical Indentation in Elastoplastic Materials : Modeling and Simulation. (2005).

26. Paietta, R. C., Campbell, S. E. & Ferguson, V. L. Influences of spherical tip radius, contact depth, and contact area on nanoindentation properties of bone. Journal of Biomechanics **44,** 285–290 (2011).

27. Noël, C. F. O., Charles, I. & Cnrs, S. Extension of the Hertz model for accounting to surface tension in nano- indentation tests of soft materials. Assessment 13–17 (2007).

28. Liao, Q., Huang, J., Zhu, T., Xiong, C. & Fang, J. A hybrid model to determine mechanical properties of soft polymers by nanoindentation. Mechanics of Materials **42,** 1043–1047 (2010).

29. Carrillo, F. et al. Nanoindentation of polydimethylsiloxane elastomers: Effect of crosslinking, work of adhesion,and fluid environment on elastic modulus. Journal of Materials Research **21,** 535–537 (2006).

30. Wei, J., McFarlin, B. L. & Wagoner Johnson, A. J. A multi-indent approach to detect the surface of soft materials during nanoindentation. Journal of Materials Research **31,** 2672–2685 (2016).

31. Sangha, H. K. Elastic-anisotropic properties of the porcine superflexor tendon measured by instrumented indentation. university of illinois at urbana champaign **53,** (2013).

32. Docking, S. Relationship between compressive loading and ECM changes in tendons. Muscles, Ligaments and Tendons Journal **3,** 7–11 (2013).

33. Chardon, M. K., Dhaher, Y. Y., Suresh, N. I., Jaramillo, G. & Zev Rymer, W. Estimation of musculotendon kinematics under controlled tendon indentation. Journal of Biomechanics **48,** 3577–3585 (2015).

34. Farine, M. Instrumented Indentation of Soft Materials and Biological Tissues. (2013).

35. Lau, T. Y. et al. Quantification of Rat Cervical Microstructure using Fourier Transform-Second-Harmonic Generation Imaging. Cleo: 2013 **1,** AW1I.3 (2013).

36. Myers, K. M. et al. A continuous fiber distribution material model for human cervical tissue. Journal of Biomechanics **48,** 1533–1540 (2015).

CHAPTER 5: A METHOD TO CHOOSE CORRECT TIP SIZE BASED ON THE FIBER DIMENSION AND STRUCTURE

5.1 INTRODUCTION

Biological tissues, including cervix and tendon, are fiber-reinforced soft tissues. Such tissues can be described as composites with a homogeneous isotropic solid matrix in which collagen fibers are distributed.[1–3] Natural tissues are hierarchically structured materials that exhibit varying structural and mechanical characteristics in fibers over a range of length scales.[4–6] As a consequence of the varied structure, tissues exhibit a diversity of mechanical properties depending on length scale.

Previous research has used a variety of tip sizes and reported indentation moduli of the same tissue within a wide range.[7–9] The size of the tip may influence results regarding indentation modulus; thus, the selection of the tip size is critical in terms of its association with the underlying fiber distribution structures.

This chapter has two purposes. The first is to exemplify the application of the MIA and non-circular contact correction to indentation experiments. The second is to illustrate that changes in tip size can lead to different indentation results. The chapter also provides guidelines for selecting the tip and designing the indentation experiment based on the fiber dimensions and distributions. The research for this chapter used two spherical tip sizes: one with a 9-um radius and the other with a 100-um radius. Porcine digital flexor tendons were prepared in multiple fiber orientations to illustrate the different interactions between the tip and the material structure.

5.2 SAMPLE PREPARATION AND EXPERIMENTS

5.2.2 Porcine flexor tendon sample preparation for indentation

Porcine flexor tendons were cut in three distinct fiber orientations at Φ = 0°, 45°, and 90°. Section 4.3.2 details the preparation procedure.

5.2.3 Porcine flexor tendon sample preparation for SHG imaging

Tendon samples for SHG imaging were sliced with Cryostat (Leica CM3050 S Research Cryostat, Leica Bio-systems, Nussloch, Germany) at a 50-um thickness as described in Section 4.3.2. The slice of tissue was sandwiched between a 3'-by-1' glass microscope slide, with a 0.8'-by-0.8' glass cover slip. Transparent coating glue was spread along the edges of the cover slide to prevent dehydration of the sample.

5.2.4 Indentation tests with a 100-um radius spherical tip with Hysitron indenter

The Hysitron Triboindenter was utilized for indentation tests on the tendon samples with a 100-um radius spherical tip. The Hysitron Triboindeter is an instrumented indenter and has been introduced in Section 1.2. It was originally designed for indentation on hard materials. In Chapter 3, we developed the MIA, which can use this indenter to perform indentation on soft materials[10]. The 100-um radius indentation tests were conducted with displacement control following the two consecutive load-unload cycles at 4-um and 8-um indentation depths, respectively. The displacement rate for this work was 2um/s. Three samples were tested for each fiber orientation of Φ=0°, 45°, and 90°. The angle Φ is the angle between the fiber direction and loading direction in indentation, and it has been defined in Chapter 4, Section 4.2, Figure 2. The indentations were performed in a one-by-three matrix in each sample (N=9, 3 samples in total) with at least 500um between two neighboring indents.

5.2.5 Indentation tests with 9-um radius spherical tip with Piuma indentor

The Piuma Nanoindenter was employed for indentation tests on the tendon samples using a 9-um radius spherical tip. The Piuma Nanoindenter is an AFM-based indenter and has been

introduced in Section 1.2. In this study, we conducted indentation tests in displacement control following the two load-unload cycles at 6-um and 8-um indentation depths with Piuma indenter, respectively, in order to calculate indentation modules from MIA described in Chapter 3. The displacement rate in this section was set at 2um/s in order to match the rate for the Hysitron indentation tests. Three samples were tested for the fiber orientations of Φ=0°, 45°, and 90°, and the indentations were performed in a three-by-three matrix on the sample surface with 500um between two neighboring locations.

5.2.6 SHG imaging and image analysis on fibril diameter

Second-harmonic generation images for fibril dimension analysis were scanned for an area of 10-by-10 um at a resolution of one-by-one pixel for one imaging frame in order to view individual fibrils. The images for collagen fiber and fascicle dimension analysis were scanned for an area of 500-by-600 um with a 50-by-50 pixel imaging frame. Each pixel was 23.15nm in SHG imaging.

The fibril dimension analysis was carried out through ImageJ. Specifically, a line was drawn along the transverse directions of the fibrils (see Figure 19B), and the average diameter of the fibrils was evaluated along the line. ImageJ evaluated the pixel intensity along the white line, and the peak width indicates the diameter of an individual fibril. The fascicle dimensions were measured by tracing the boundaries between the two fascicles, which encompassed a narrow black region that represents the isotropic area (see Figure 19C) between the two green regions, which symbolize the collagen bundles with a strong direction alignment (see Figure 19C). The contact areas of the 9-um, 100-um, and 500-um radius tip sizes at 8-um indentation depth were calculated and compared with the dimensions of the fiber components, and two from the three

were selected to perform indentation with Piuma indenter to calculate the young's modulus of the tendon tissue.

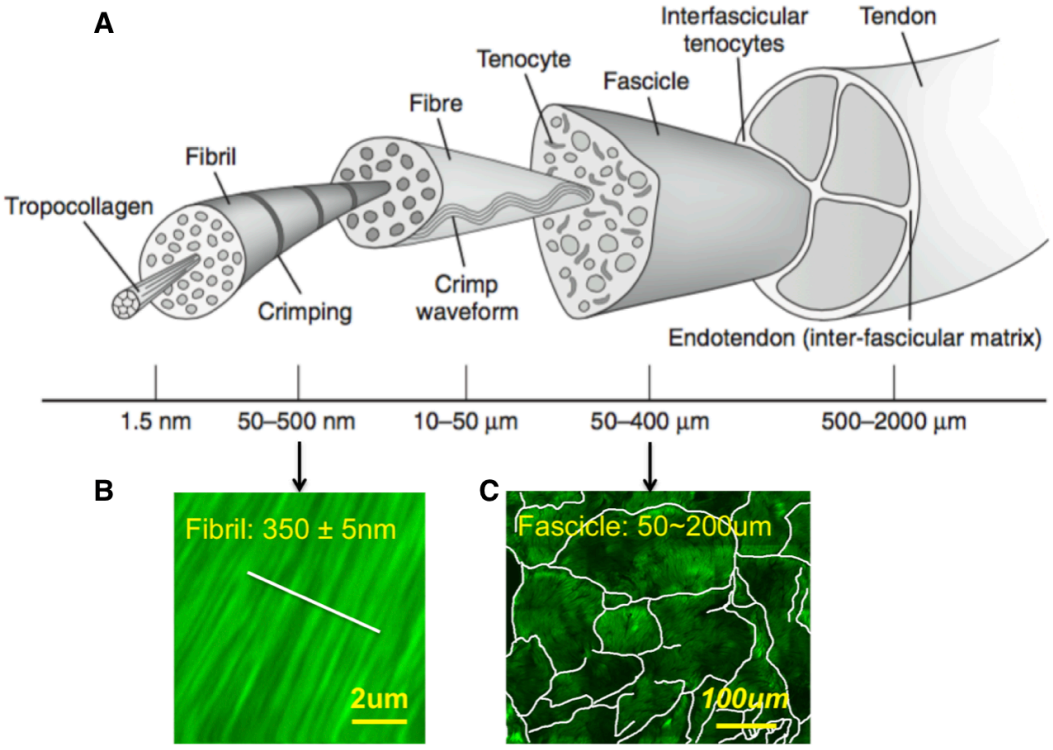

Figure 19 (A) Tendon anatomy as adapted from (refs) was used to summarize the length scales of the fiber components in the tendon tissue; (B) evaluation of the average ± standard deviation of fibril diameter in the porcine flexor tendon from a transverse section, with the white line indicating the range of evaluation; (C) fascicle boundaries (white lines) from a longitudinal section illustrating the range of fascicle sizes

5.3 ANALYSIS OF THE INDENTATION RESULTS

The analysis of the indentation results involves the methods on which Chapters 3 and 4 have elaborated. The MIA for Hertzian contact theory (Chapter 3) was employed to obtain the indentation moduli through the Piuma indenter in this study. The moduli were measured by the MIA at the same tip size but different orientations, Φ, and analyzed with a one-way ANOVA and post-hoc Tukey test. Next, the non-circular contact correction (see Chapter 4) adjusted the estimation of the contact area between the spherical tip and anisotropic material. The corrected

and uncorrected contact areas were compared. An estimation of the correction factor, or RCA, was derived from Figure 10 in Chapter 4. Both Figure 19A and 19B in the current chapter were directly obtained from Figure 15B, and Figure 18 in Chapter 4.

5.4 RESULTS AND DISCUSSION

This section reports the results for the indentation moduli of the samples of porcine tendon at three fiber orientations (Φ = 0°, 45°, and 90°) as measured with two tip sizes, namely with 9-um and 100-um radii. The dimensions of the fiber components were also measured to illuminate the regions inside the fibers with which different tips were possibly in contact. This section concludes by discussing possible sources of difference between the results from the various tip sizes and demonstrating the importance of tip size selection.

5.4.1 The indentation moduli obtained using two tips sizes

Figures 20A and 20B contain representative data for the loading curves for 4-um indentations and the respective Hertzian fits.

Figure 20B depicts only one curve, the Φ = 90 orientation, since the curves overlap at different fiber orientations for the 9-um indenter. Figure 20C reports the values of indentation moduli at the three fiber orientations as determined by the MIA and with the two tip sizes. There was a statistically significant difference in modulus for each of the three fiber orientations when measured with the 100-um tip ($P<0.05$). In contrast, there was no statistically significant difference in modulus for each of the three fiber orientations when measured with the 9-um tip ($P>0.05$).

The correction for non-circular contact was then made on the indentation moduli obtained from the MIA and the Hertzian fit using the piuma indenter, and Figure 21 presents the results. The one-way ANOVA and post-hoc Tukey test reflect that the corrected indentation moduli at

various fiber orientations were also significantly different ($P<0.05$). The difference between the corrected and uncorrected values measured with the Piuma indenter at $\Phi = 90°$, 45°, and 0° were 3.6%, 2.2%, and 0%, respectively.

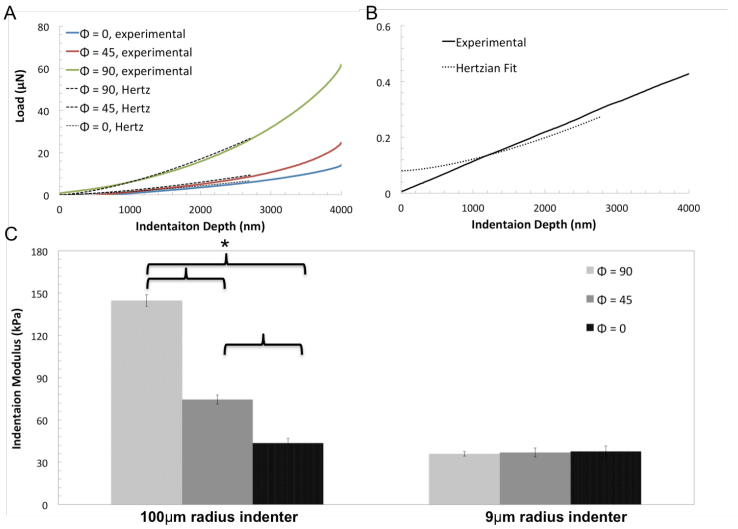

Figure 20. Indentation modulus obtained through the MIA and 100-um and 9-um radius spherical tips; (A, B) loading curve and Hertzian fit from the three fiber orientations; (B) depicts only one experimental curve because the curves overlap for the three fiber orientations for indentation with the 9-um tip; (C) indentation modulus obtained through the MIA and the two tip sizes; the modulus measured at each orientation for the 100-um radius tip was significantly different ($p<0.05$); no significant difference in modulus emerged between orientations for the 9-um radius tip ($p>0.05$).

The moduli for different fiber orientations differed when measured with the 9-um spherical tip but not with the 100-um spherical tip. This paragraph discussed the mechanical response of the tendon under indentation as a composite of the solid matrix with elastic fibers bundles, and the fibers do not mechanically respond under compression. Indentation was a compression-tension mixed behavior. The region of contact was under compression, and the region out of contact near the indenter was under tension[18]. Loading the tendon at $\Phi = 0°$ (longitudinal loading, see loading direction in Chapter 4, Figure 11) induced compression along the fiber, and the tension was induced transversely to the fiber orientation. Since the fibers did not take the load under compression when the compressive load was along the fiber, indentation

modulus should thus reflect the modulus of the solid matrix only. As the fibers rotate toward Φ = 90°, the tension was induced in along the fiber; thus, the fibers were gradually stretched along the longitudinal direction during indentation. Because of the differing levels of fiber responses at various Φ, the indentation modulus should be the smallest when Φ=0° and largest when Φ= 90°.

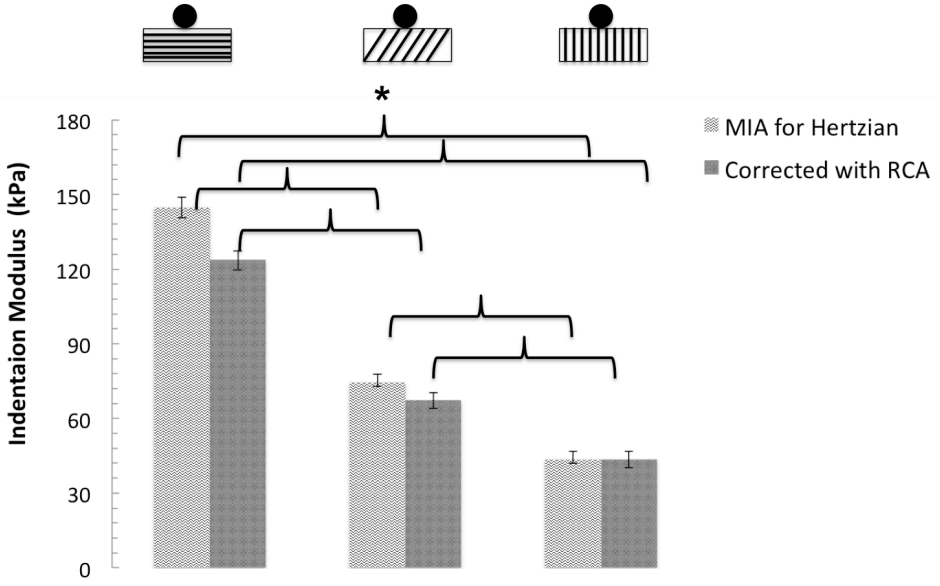

Figure 21. Indentation moduli with and without non-circular corrections at different fiber orientations; statistical analyses indicate that indentation moduli differ significantly by fiber orientation with both corrected and non-corrected results, and there is also a significant difference between the corrected and non-corrected results at Φ = 90° and 45°.

The results in Figure 21 reflect the above discussion. More transversely oriented fibers corresponded to greater overestimation of the indentation modulus by the circular approximation. After the non-circular corrections, the statistical analyses still highlighted differences in indentation moduli between fiber orientations. Previous studies have also used a spherical tip or circular punch to indent multiple fiber orientations of the tendon, and their results showed

statistical differences.[11–13] However, all the tip sizes that they have used have been considered large, ranging between 500um and 1mm.

Possible reasons that the 9-um tip could not detect the differences in moduli between orientations include the following. Firstly, 9-um radius tip with 8um indentation depth likely exceeds the small/infinitesimal deformation zone, thus, theory of infinitesimal elastic deformation no longer applies under this case. Secondly, the small spherical tip with 9-um radius will result in high noise to signal ratio, and thus varied the test results. Moreover, the 9-um radius tip could only cause local deformation of the fiber, rather than a fiber-scale tensile behavior; since the fibers were crimpled at zero-load status, an initial load was needed to straighten the fibers in order to stretch them. A last possibility is that the material that was in contact with this small size of the tip was homogenous at that length scale. These possibilities motivate a study of the dimensions of the collagen fiber components and the contact area under different tip sizes in relation to the fiber dimensions.

5.4.2 Tip sizes effects in relation to the dimensions of fiber components

Figure 19A illustrates the tendon anatomy from a paper by James H. and C. Wang.[14] The figure summarizes the length scale of the fiber components in the tendon tissue. Figure 19B depicts the measurement of the average diameter of the fibrils from the sample with fibers oriented transversely. An individual fibril was measured as 15 pixels or 350nm. The white line in Figure 19C indicates the fascicle boundaries, which were recognized from the image of a tendon sample with longitudinally oriented fibers. The dimensions of the fascicles differ by location, and the range of fascicle diameter was 50um to 200um.

Figure 22A plots the Hertzian contact area under 9-um, 100-um, and 500-um radius spherical tips at 8-um indentation depth, from which 2 tip sizes were selected for the followed

indentation tests. Figure 22B gives the non-circular contact correction factor RCA, which was obtained from Figure 15 in Chapter 4. Figure 22C, 22D, and 22E illustrates the relative size of the corrected contact areas under the tip sizes compared with the fiber structures at 8-um indentation depth.

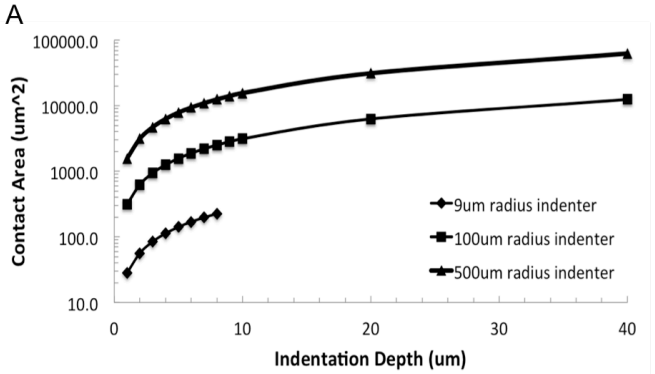

B

Fiber Orientation	RCA
Transverse	1.11
45 degree	1.06
Vertical	1

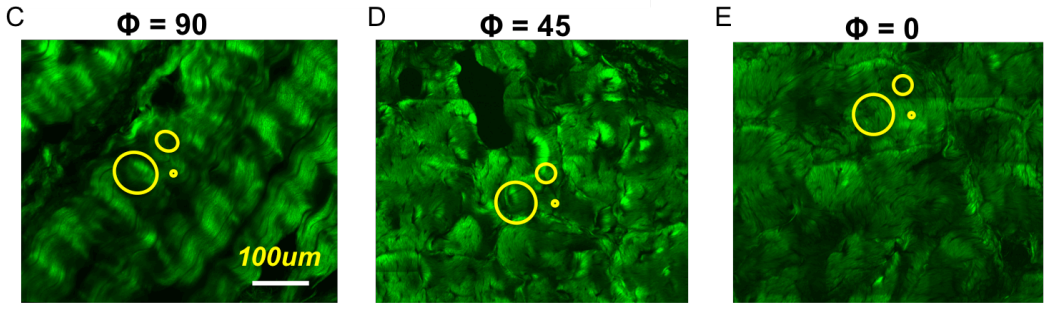

Figure 22 (A) Contact area as a function of indentation depth for three tip sizes (9-um, 100-um, and 500-um radius) based on the Hertzian contact solution; (B) correction factors for Φ= 0°, 45°, and 90° as obtained from Figure 1; (C, D, E) the SHG images of porcine flexor tendon at Φ= 0°, 45°, and 90°. The yellow ellipses demonstrate the size of the contact area under 9-um, 100-um, and 500-um radius spherical tips at 8-um indentation depth after consideration of the non-circular contact correction; C, D, and E also illustrate the relative sizes of the contact areas compared to the fiber structures and length scales.

The 100-um radius tip was in contact with collagen fiber bundles, and the 500-um radius tip was in contact with even more collagen fiber bundles, as Figure 22C indicates. However, both tips were in contact within a fascicle, as Figure 22E reveals. The 9-um radius tip was in contact with multiple fibrils within a collagen fiber, as Figure 22C demonstrates.

The dimension of the fibrils and fascicles as measured from the porcine digital flexor tendons was within the range of those reported by previous studies. This measurement was

important because the dimensions of the fiber components vary from tissue to tissue and are usually associated with tissue functions.

With the measured fiber component dimensions, we discuss the three possibilities that have been mentioned in the last paragraph of Section 4.1. Since the structure under contact for 100-um and 500-um radius tips were similar, i.e. within a fascicle, but in contact with multiple collagen fiber bundles, it was appropriate to assume that the AR of contact that the two tips made was the same and thus the results in Chapter 4 could be used. The 9-um radius tip was in contact within a collagen fiber with multiple fibrils, and it was not known whether the AR of contact under the 9-um radius tip could be assumed to be the same as that under the 500-um radius tip.

In order to examine the possibilities of force differences at different fiber orientations, the corrected indentation moduli measured from 100-um radius indenter were referenced. Based on Equation 54 in Chapter 4, the theoretical load for Φ= 0°, 45°, and 90° were 1.08uN, 0.89uN, and 0.54uN, respectively. The minimum force resolution that Piuma Nanoindenter can sense is 20pN; thus, if the experiments were carried out ideally, the current load measurement capability would be able to sense this difference. However, this experiment involved multiple factors that could introduce errors and increase the difficulty of the experiment. The surface roughness poses one of the most significant problems, the rougher the surface is, the lower force is needed to reach an 8-um indentation depth (since the actual contact area will be smaller), and will thus result in a lower indentation modulus. In this study, even though we processed our sample surfaces carefully at 50-um smoothening steps, the surface could not be flat in the scale of a couple fibrils (350nm in diameter for each fibril). This roughness could potentially affect the results from the 9-um radius tip, as the roughness was about 10% of the contact radius. In contrast, for the 100-um radius tip, this roughness was less than 1%. This roughness may have introduced errors to the

measurements from the 9-um radius tip that could have resulted in the lack of significant differences in the results between fiber orientations.

Figure 22C indicates that the fibers were crimped, and an initial force was needed in order to pre-stretch them. This value of the preload can be evaluated from the solid matrix properties and the fiber crimp level. This initial force has not been previously reported, but the region of the tendons under uniaxial tensile tests were usually evaluated at 1% of the strain.[15–17] Thus, we assumed that 1% strain was needed in the solid matrix in the longitudinal direction of the fibers in order to pre-stretch the fibers, so the required stress along the longitudinal fiber orientation was 1%*70kPa, or 0.7kPa. A finite element analysis simulation was performed as described in Chapters 3 and 4, with the modulus of the solid matrix input into the isotropic material model. The force needed to generate a 0.4kPa stress, or 1% strain in fiber direction at transverse orientation, was 0.7uN. The maximum load at 8um was 0.88uN, as Figure 20B notes, which can possibly explain why no differences emerged among the moduli of different fiber orientations that were measured under the 9-um radius tip. When the fibers could not be pre-stretched despite the direction of their rotation, the indentation modulus that we measured was the modulus of the isotropic solid matrix.

The findings above demonstrate that future studies on indentation of soft biological tissues must understand the fiber characteristics in order to choose a tip that enables the measurement of differences between tissue locations. The major factors that can inform tip selection are the dimensions of the fibrils, collagen fibers, and collagen fiber bundles as well as the nonlinearity (i.e. crimping level) of the fibers. With the tip selection studies described in Chapter 5, a procedure is listed below to study anisotropic but locally transversely-isotropic materials following what was described in 4.4.3.

Firstly, the fiber component length scales in the tissue allow for an estimate of the structure in which the tip is in contact. Additionally, the surface structure roughness that the fiber length scale contributes is necessary to consider. Studies should employ tips that can make sufficiently large contact radii to overcome this roughness. Studies can overcome this surface roughness by selecting an appropriate tip size and a suitable indentation depth that is based on such tip size.[18,19]

Then, we need to understand the fiber distribution orientations, and make stamping marks on material surfaces at the interested fiber orientation, in order to know the contact area at a certain depth with a certain fiber orientation. With the information of the contact area from the stamping marks, we can calculate AR and RCA as described in Section 4.3 and Section 4.4 respectively.

5.5 CONCLUSIONS

This study has compared three tip sizes with regard to the indentation depth, selected two of the tips that gave consistent measuring result, and reported indentation moduli that were measured by two selected spherical tip sizes. Using the 100-um radius spherical tip, we were able to detect differences in indentation modulus at different fiber orientations, whereas we could not when using the 9-um radius spherical tip. The possible reasons were as follows. On the one hand, the surface roughness on the order of several fibril diameters can result in large errors when using the 9-um radius tip. On the other hand, 9-um radius tip with 8um indentation depth likely exceeds the small/infinitesimal deformation zone, thus, theory of infinitesimal elastic deformation no longer applies under this case. This study concludes the major factors that can affect tip selection and offers guidance for choosing the right tip size based on the fiber dimension and structure.

5.6 LIMITATIONS

This study used Hertzian contact theory, which is based on an assumption of linear elasticity, as discussed in this chapter, a small tip size with a large indentation depth will no longer fit into the linear elastic Hertzian theory, a model that allows large deformation need to be developed to simulate the test with small tip.

Surface roughness need to be considered in future study, since this be critical for determining a good and small tip size and corresponding indentation depth. If tip size and depth selection are not enough to make full contact with the material surface, the indentation modulus will be underestimated.

In this study, since the collagen fibers were densely packed, the fiber dispersion ratio, and fiber density was not considered changing throughout the whole tissue. However, in many other tissues, such as that of the cervix,[20–22] collagen fibers are not as densely packed as they are in tendon, so the dispersion ratio and density of the fibers would vary from location to location in the tissue, and the factors mentioned above were not considered in this study.

5.7 REFERENCES

1. Myers, K. M., Cone, F. & Quigley, H. Mechanics of Biological Systems and Materials, Volume 2. **2,** 87–92 (2011).
2. Bierbaum, S., Hintze, V. & Scharnweber, D. Functionalization of biomaterials surfaces using artificial extracellular matrices. Biomatter **2,** 132–141 (2012).
3. Gasser, T. C., Ogden, R. W. & Holzapfel, G. A. Hyperelastic modelling of arterial layers with distributed collagen fibre orientations. Journal of The Royal Society Interface **3,** 15–35 (2006).
4. Docking, S. Relationship between compressive loading and ECM changes in tendons.

Muscles, Ligaments and Tendons Journal **3,** 7–11 (2013).

5. Badylak, S. F., Freytes, D. O. & Gilbert, T. W. Extracellular matrix as a biological scaffold material: Structure and function. Acta Biomaterialia **5,** 1–13 (2009).
6. Zhu, D. & Barthelat, F. Mechanics of Biological Systems and Materials, Volume 2. Experimental Mechanics **2,** 181–187 (2011).
7. Chardon, M. K., Rymer, W. Z. & Suresh, N. L. Quantifying the deep tendon reflex using varying tendon indentation depths: Applications to spasticity. IEEE Transactions on Neural Systems and Rehabilitation Engineering **22,** 280–289 (2014).
8. Sangha, H. K. Elastic-anisotropic properties of the porcine superflexor tendon measured by instrumented indentation. university of illinois at urbana champaign **53,** (2013).
9. Spiesz, E. M., Roschger, P. & Zysset, P. K. Elastic anisotropy of uniaxial mineralized collagen fibers measured using two-directional indentation. Effects of hydration state and indentation depth. Journal of the mechanical behavior of biomedical materials **12,** 20–8 (2012).
10. Lin, D. C., Shreiber, D. I., Dimitriadis, E. K. & Horkay, F. Spherical indentation of soft matter beyond the Hertzian regime: Numerical and experimental validation of hyperelastic models. Biomechanics and Modeling in Mechanobiology **8,** 345–358 (2009).
11. Samuel Salisbury, S. T., Paul Buckley, C. & Zavatsky, A. B. Transverse Compression of Tendons. Journal of biomechanical engineering **138,** 41002 (2016).
12. Aifantis, K. E., Shrivastava, S. & Odegard, G. M. Transverse mechanical properties of collagen fibers from nanoindentation. Journal of materials science. Materials in medicine **22,** 1375–81 (2011).
13. Paul Buckley, C., Samuel Salisbury, S. T. & Zavatsky, A. B. Viscoelasticity of Tendons

Under Transverse Compression. Journal of Biomechanical Engineering **138,** 101004 (2016).

14. Wang, J. H. C. Mechanobiology of tendon. Journal of Biomechanics **39,** 1563–1582 (2006).

15. Khayyeri, H., Longo, G., Gustafsson, A. & Isaksson, H. Comparison of structural anisotropic soft tissue models for simulating Achilles tendon tensile behaviour. Journal of the Mechanical Behavior of Biomedical Materials **61,** 431–443 (2016).

16. Feng, Z., Tateishi, Y., Nomura, Y., Kitajima, T. & Nakamura, T. Construction of fibroblast-collagen gels with orientated fibrils induced by static or dynamic stress: Toward the fabrication of small tendon grafts. Journal of Artificial Organs **9,** 220–225 (2006).

17. Han, W. M. et al. Macro- to microscale strain transfer in fibrous tissues is heterogeneous and tissue-specific. Biophysical Journal **105,** 807–817 (2013).

18. Paietta, R. C., Campbell, S. E. & Ferguson, V. L. Influences of spherical tip radius, contact depth, and contact area on nanoindentation properties of bone. Journal of Biomechanics **44,** 285–290 (2011).

19. Buffinton, C. M., Tong, K. J., Blaho, R. A., Buffinton, E. M. & Ebenstein, D. M. Comparison of mechanical testing methods for biomaterials: Pipette aspiration, nanoindentation, and macroscale testing. Journal of the mechanical behavior of biomedical materials **51,** 367–79 (2015).

20. Yao, W. et al. Collagen fiber orientation and dispersion in the upper cervix of non-pregnant and pregnant women. PLoS ONE **11,** 1–20 (2016).

21. Poellmann, M. J., Chien, E. K., McFarlin, B. L. & Johnson, A. J. W. Mechanical and structural changes of the rat cervix in late-stage pregnancy. Journal of the Mechanical

Behavior of Biomedical Materials **17,** 66–75 (2012).

22. Lau, T. Y. et al. Application of Fourier transform-second-harmonic generation imaging to the rat cervix. Journal of Microscopy **251,** 77–83 (2013).

CHAPTER 6: SUMMARY AND FUTURE WORKS

6.1 THESIS SUMMARY

This thesis has introduced a series of methods to correctly design and analyze indentation experiments on soft materials and anisotropic biological tissues. It has specifically addressed challenges of indentation with soft biological materials.

Chapter 3 has addressed a surface detection obstacle that complicates indentation on soft material. The novel MIA method has been developed and presented in order to detect the sample surface and thus be able to obtain material properties from indentation tests. This method has been developed with consultation of both the Oliver-Pharr model and the Hertzian model.

Chapter 4 has focused on a non-circular contact challenge that hinders accurate estimation of the indentation modulus. It has developed a simple experimental method for estimating the true contact area as well as a more accurate indentation modulus. This method facilitates simple multiplication of a correction factor to allow for correction of the indentation modulus that results from the circular contact approximation.

Chapter 5 has discussed the challenge of choosing the correct tip size for a particular fiber structure. This chapter has exemplified the application of the MIA and non-circular contact correction to the indentation tests and provided an experimental protocol and guideline for selecting a suitable tip size.

6.2 FUTURE WORKS

Mechanobiological modeling of biological tissues has widely adopted computational approaches to predict tissue differentiation and improve understandings of both mechanical and

biological mechanisms.[1–3] Continuum constitutive models, such as the Gasser-Ogden-Hassel model,[4] the Yeoh model,[2] and the Mooney-Revlin model[5], merit development or study for the quasi-static properties of biological tissues in the future.

The next step is to examine a more heterogeneous fibrous tissue – rat cervical tissue – with the methods and theories in Chapters 3 through 5. The rat cervical tissue can be imaged by SHG through the entire cross-section and digitally segregated into zones according to the fiber distribution characteristics. The fibril size and regions of interest can be measured to inform spherical tip selection. A steel bead can be selected accordingly in order to perform the non-circular contact correction measurements. The loading curves can be studied with both the Hertzian fit, as this chapter has done, and the hyperelastic constitutive model.

A suitable tip size can be selected on the basis of the fibril size in each zone. By following the previous steps, the loading part of loading-unloading curves can be studied in terms of both Hertzian fit and the hyperelastic constitutive model. The implementation of the hyperelastic model is under development.

6.3 REFERENCES

1. Myers, K. M. et al. A continuous fiber distribution material model for human cervical tissue. Journal of Biomechanics **48,** 1533–1540 (2015).
2. Lin, D. C., Shreiber, D. I., Dimitriadis, E. K. & Horkay, F. Spherical indentation of soft matter beyond the Hertzian regime: Numerical and experimental validation of hyperelastic models. Biomechanics and Modeling in Mechanobiology **8,** 345–358 (2009).
3. Gasser, T. C., Ogden, R. W. & Holzapfel, G. A. Hyperelastic modelling of arterial layers with distributed collagen fibre orientations. 15–35 (2006). doi:10.1098/rsif.2005.0073
4. Gasser, T. C., Ogden, R. W. & Holzapfel, G. A. Hyperelastic modelling of arterial layers

with distributed collagen fibre orientations. Journal of The Royal Society Interface **3,** 15–35 (2006).

5. Torres, F. G., Troncoso, O. P., Piaggio, F. & Hijar, A. Structure-property relationships of a biopolymer network: the eggshell membrane. Acta biomaterialia **6,** 3687–93 (2010).